

Molecular Electronic Transducer-Based Seismometer and Accelerometer
Fabricated With Micro-Electro-Mechanical Systems Techniques

by

Hai Huang

A Dissertation Presented in Partial Fulfillment
of the Requirements for the Degree
Doctor of Philosophy

Approved April 2014 by the
Graduate Supervisory Committee:

Hongyu Yu, Chair
Lenore Dai
Jennie Si
Hanqing Jiang

ARIZONA STATE UNIVERSITY

May 2014

ABSTRACT

This thesis presents approaches to develop micro seismometers and accelerometers based on molecular electronic transducers (MET) technology using MicroElectroMechanical Systems (MEMS) techniques. MET is a technology applied in seismic instrumentation that proves highly beneficial to planetary seismology. It consists of an electrochemical cell that senses the movement of liquid electrolyte between electrodes by converting it to the output current. MET seismometers have advantages of high sensitivity, low noise floor, small size, absence of fragile mechanical moving parts and independence on the direction of sensitivity axis. By using MEMS techniques, a micro MET seismometer is developed with inter-electrode spacing close to $1\mu\text{m}$, which improves the sensitivity of fabricated device to above $3000\text{ V}/(\text{m}/\text{s}^2)$ under operating bias of 600 mV and input acceleration of $400\text{ }\mu\text{G}$ ($G = 9.81\text{ m}/\text{s}^2$) at 0.32 Hz. The lowered hydrodynamic resistance by increasing the number of channels improves the self-noise to -127 dB equivalent to $44\text{ nG}/\sqrt{\text{Hz}}$ at 1 Hz. An alternative approach to build the sensing element of MEMS MET seismometer using SOI process is also presented in this thesis. The significantly increased number of channels is expected to improve the noise performance.

Inspired by the advantages of combining MET and MEMS technologies on the development of seismometer, a low frequency accelerometer utilizing MET technology with post-CMOS-compatible fabrication processes is developed. In the fabricated accelerometer, the complicated fabrication of mass-spring system in solid-state MEMS accelerometer is replaced with a much simpler post-CMOS-compatible process containing only deposition of a four-electrode MET structure on a planar substrate, and a

liquid inertia mass of an electrolyte droplet encapsulated by oil film. The fabrication process does not involve focused ion beam milling which is used in the micro MET seismometer fabrication, thus the cost is lowered. Furthermore, the planar structure and the novel idea of using an oil film as the sealing diaphragm eliminate the complicated three-dimensional packaging of the seismometer. The fabricated device achieves 10.8 V/G sensitivity at 20 Hz with nearly flat response over the frequency range from 1 Hz to 50 Hz, and a low noise floor of $75 \mu\text{G}/\sqrt{\text{Hz}}$ at 20 Hz.

DEDICATION

This thesis is dedicated to my parents who raised me with so much love.

And to my dear wife who is, and will be always there with me.

ACKNOWLEDGMENTS

This thesis would not have been finished without the support, inspiration and enthusiasm of many people. The most important one is my advisor, Prof. Hongyu Yu. It was he who gave me the chance to join this spectacular project in the world of MEMS, which is supported by NASA-PIDDP-NNX10AL25G. His support, patience and friendship helped me go through some of the most difficult times in my PhD career. He is a mentor who not only expands my knowledge in terms of research, but also leads me into the right direction in my personal growth. I am extremely grateful for his guidance and support throughout the research.

It was really enjoyable to work with my group, Xiaotun, Rui, Yong, Teng, Bryce, Jon and Mengbing. There are so many times we worked together in the cleanroom until late night. We shared our joy of success and sad of failure. One thing always in our mind is that we will never give up. I will never forget Rui, Bryce and Jon who helped me fabricated some of the most critical steps in my project while I was sick. Without you, I won't publish my first journal paper. Thank you so much!

Outside the group, I would like to thank Dr. Jiang who gave me many useful suggestions on research and support me as my committee member, thank Prof. Si who clarified me with the transitions between time and frequency domain on differential equations, thank Dr. Dai who gave me guidance on the viscosity of the electrolyte and a chance to use a state-of-art instrument in her lab to characterize it, thank Dr. Vadim Agavonov and his team in Moscow who helped us assemble and test the fabricated seismometer sensing cell, thank Qian Zhang for helping with the rotated Pt deposition in

USC. Also I would like to thank my dear friends, Hongwei, Zeming and many others who brought me so much fun during my PhD life.

Finally I would like to thank my parents and my dear wife who have influenced me throughout my life.

TABLE OF CONTENTS

	Page
LIST OF TABLES	ix
LIST OF FIGURES	x
CHAPTER	
1 INTRODUCTION	1
1.1 SEISMOLOGY AND SEISMOMETERS	1
1.1.1 APPLICATIONS	2
1.1.2 STATE-OF-ART SEISMOMETERS	8
1.2 MEMS CAPACITIVE ACCELEROMETERS	11
1.3 BASIC WORKING PRINCIPLES OF THE MASS-SPRING SYSTEM IN SEISMOMETERS	17
1.3.1 FREQUENCY RESPONSE	18
1.3.2 NOISE	22
2 MOTION SENSORS BASED ON MOLECULAR ELECTRONIC TRANSDUCER	23
2.1 MOLECULAR ELECTRONIC TRANSDUCER- PRINCIPLE OF OPERATION	24
2.2 TRANSFER FUNCTION	28
2.3 FEEDBACK SUBSYSTEM	31
2.4 NOISE	32
2.4.1 THERMOHYDRODYNAMIC SELF-NOISE	32
2.4.2 CONVECTION-INDUCED SELF-NOISE	33

CHAPTER	Page
2.4.3 GEOMETRY SELF-NOISE	34
2.4.4 SHOT NOISE	34
2.4.5 ELECTRONIC SELF-NOISE	35
2.5 DIFFERENT TYPES OF MET MOTION SENSOR	36
3 MICRO SEISMOMETER BASED ON MOLECULAR ELECTRONIC TRANSDUCER TECHNOLOGY FOR PLANETARY EXPLORATION	40
3.1 MEMS SENSING ELEMENT FABRICATION	42
3.1.1 PHOTORESIST AS SELF-ALIGNMENT MASK FOR MULTI-LAYER THIN FILM DEPOSITION	42
3.1.2 MECHANICAL MICRO-MILLING MACHINE	45
3.1.3 FOCUSE ION BEAM	46
3.2 EXPERIMENTAL RESULTS AND DISCUSSION	51
3.2.1 SENSITIVITY	51
3.2.2 LINEARITY	54
3.2.3 NOISE	55
4 ALTERNATIVE FABRICATION METHODS OF MICRO SEISMOMETER BASED ON MOLECULAR ELECTRONIC TRANSDUCER USING SILICON ON INSULATOR PROCESS TECHNOLOGY	57
4.1 SINGLE-SOI FABRICATION PROCESS	58
4.2 DOUBLE-SOI FABRICATION PROCESS	60

CHAPTER	Page
5 MET-BASED LOW FREQUENCY ACCELEROMETER WITH POST-CMOS COMPATIBLE PROCESS USING DROPLET AS SENSING BODY	64
5.1 DEVICE FABRICATION	66
5.2 OPERATION PRINCIPLE	67
5.3 EXPERIMENTAL RESULTS	70
6 SUMMARY AND FUTURE WORK	74
6.1 EXPERIMENT SETUP.....	75
6.2 MET SENSOR PACKAGING	77
6.3 THEORITICAL STUDY OF MET PRINCIPLE.....	79
REFERENCES	80
APPENDIX	85
A.1 MICRO-FABRICATION PROCESS FOR MICRO MET SEISMOMETER INVOLVING FIB.....	86
A.2 MICRO-FABRICATION PROCESS FOR MICRO MET SEISMOMETER USING DOUBLE-SOI SUBSTRATE	88

LIST OF TABLES

Table	Page
1. Parameters of state-of-art solid-state mass-spring based seismometers.....	11
2. Comparisons of MEMS capacitive accelerometers from research groups and commercialized products	15
3. Current performance parameters for linear MET seismic sensors	38
4. Current performance parameters for MET rotational seismometers.....	39
5. Sensing cell parameters for the MEMS MET seismometer	42
6. Configurations of three fabricated MEMS MET seismometers.....	52
7. Scale factor vs. acceleration	55

LIST OF FIGURES

Figure	Page
1. Replica of Zhang Heng's seismoscope “Houfeng Didong Yi”	3
2. Commercialized state-of-art seismometers	10
3. Different types of differential capacitors.....	12
4. Sensing element of commercialized ADXL150 MEMS capacitive accelerometer	14
5. Block diagram of ADXL series accelerometer	14
6. The packaged micro seismometer by Pike, et al [31]	17
7. A schematic of an inertial seismometer based on mass-spring damper	18
8. Schematic of amplitude frequency responses for input displacement, velocity and acceleration, for a 1 Hz inductive type seismometer (velocity transducer, top), and for a 1 Hz mechanical seismometer or the output of capacitive transducer in a 1 Hz VBB seismometer (bottom).	21
9. Schematic of the basic MET sensing element	25
10. Tri-iodide ion concentration with its gradient for a MET motion sensor. (a) No external acceleration, (b) In the presence of external acceleration	27
11. A block diagram of MET motion sensor including feedback subsystem ..	32
12. Noise performance of a MET seismometer (CME-6211) in comparison with high-performance, industry-grade broadband seismometers. Red: MET seismometer CME-6211; Blue: Streckheisen STS-2 broadband seismometer; Green: Trillium T240 broadband seismometer.	36
13. Schematic of different type of MET motion sensor	37

Figure	Page
14. An assembled 3-axis linear MET seismometer including two orthogonal horizontal sensors and one vertical sensor, along with the sensing circuits	38
15. Schematic diagram of the sensing element, (a) Overview, (b) Cross-section view	42
16. (Left) Diagrams illustrating the ideal fabrication process using AZ4620 photoresist as self-alignment mask for film deposition. (Right) Due to the deposition directionality problem, multi-layers at the edge are either not straight or covered too much by the next top layer	43
17. SEM images showing the holes array and sidewalls using the E-beam evaporation and lift-off process with Su-8 2025 photoresist as self-alignment mask for thin films evaporation.....	45
18. SEM images showing the holes fabricated by physical micro-milling machine. The sample surface and holes were damaged by milling	46
19. (left) SEM images of 16 holes fabricated with FIB on the diaphragm, (right) sharp and smooth side wall of hole showing 9 layers	47
20. A schematic drawing of the finished micro seismometer sensing element (single channel)	48
21. Detailed fabrication processes for the micro seismometer based on MEMS and METs technology	50
22. Photographs (optical and SEM) of a fabricated single-50 μm diameter-channel MEMS MET seismometer core. (a) 20 batch fabricated devices on one wafer. (b) A single-50 μm diameter-channel micro MET	

Figure	Page
seismometer core. (c) SEM image of the through hole milled by FIB on the 5.8 μm thin diaphragm. (d) SEM image of the side wall of the through hole, showing exposed alternating Pt and SiN layers	50
23. Assembled sensing cell for a MEMS MET seismometer	52
24. Measurement results of sensitivity frequency response of a fabricated micro MET seismometer (device 1) in different bias conditions	53
25. Comparison of the sensitivity frequency response for three MEMS MET seismometers in different configurations. Black, device 1; Red, device 2; Blue, device 3	54
26. Noise PSD filtered in 0.01 – 50 Hz frequency range of fabricated single -50 μm diameter-channel, 20-40 μm diameter-channel and 50-40 μm diameter- channel micro MET seismometers, in comparison with CMG-40T seismometer .	55
27. Fabrication processes of the sensing element of MET based micro seismometer with single-SOI wafers.....	59
28. Fabrication processes of the sensing element of MET based micro seismometer with Double-SOI wafers	61
29. Photograph of a fabricated device with double-SOI process (a), and a SEM image showing the metal (Ti/Pt) coverage on the sidewall of the channel including silicon and the recessed SiO ₂	62
30. Schematic of a traditional MET accelerometer using standard-machined platinum mesh separated by dielectric grids as sensing cell. The sensor is manually assembled with highly-flexible rubber diaphragms	66

Figure	Page
31. Overview of the electrolyte droplet-based MET accelerometer: (a) Top view schematic of the device. (b) Sensing element of the fabricated device, (c) Zoom-in view of the droplet-covered electrodes	69
32. Microfabrication processes of the post-CMOS-compatible MEMS MET accelerometer	69
33. Experimental result of sensitivity of the device under 20 Hz sinusoidal input accelerations within 0.6G magnitude.....	72
34. Experimental result of the normalized sensitivity frequency response of the device in comparison with the theoretical analysis. Resonant frequency is down shifted to ~30Hz and ~25Hz when ~150% and ~200% electrolyte droplet volume are applied, respectively	72
35. Measured output signal spectrum under a 0.35 G sinusoidal excitation at 20 Hz (n=5), showing an input-referred noise floor of $75 \mu\text{G}/\sqrt{\text{Hz}}$	73
36. Experiment setup of the MET based micro seismometer/accelerometer....	76
37. Circuit topology for the measurement of the MET based micro seismometers and accelerometers	77
38. Packaging and assembly prototype of the MET based micro seismometer.....	78

CHAPTER 1

INTROUCTION

In this chapter, the basic idea of seismology and seismometer is introduced. The applications of seismometers mainly include earthquake study, nuclear monitoring and planetary exploration. The history of the development of seismometers is also introduced by going over some examples of early-age seismometers and traditional state-of-art seismometers. In addition, this chapter presents the efforts dedicated by people trying to miniaturize the traditional seismometers in order to expand their application fields, which is mostly based on the development of solid-state MEMS capacitive accelerometers. The working principles of solid-state seismometers and accelerometers are similar and based on mass-spring system, which is discussed in detail in the last section of this chapter.

1.1 Seismology and Seismometers

Seismology, the study of propagation of seismic waves through the surface and interior of the Earth or other planets, plays an important role in studying seismic activities and unveiling internal structure of a planet. Seismometers are instruments used in seismology that sense the motions of the ground, including displacement, velocity and acceleration. The amplitude and frequency range of seismic signals is very large. The smallest amplitude might be as small as 0.1 nm which is limited by the ground noise. The largest possible displacement may reach 10 m during an earthquake [1]. Therefore, the dynamic range is 10^{11} . Similarly, the frequency range of seismic signals starts from 0.0001 Hz to 1000 Hz. Typically, for good studies of local and global seismic activities, a

seismic station should at least cover the ground motions from 1 nm to 10 mm, and frequency range from 0.01 Hz to 100 Hz. It is not possible to make one single instrument to cover all the above displacement and frequency ranges. Seismic instruments are designed with different gains and frequency responses for application in different ranges of frequency and amplitude. They are basically categorized to short period (SP), long period (LP) and very broadband sensors (VBB) (mostly velocity broadband sensors).

1.1.1 Applications

Seismometers are designed targeting different applications mainly including studying earthquakes, nuclear detonation monitoring and planetary exploration.

1.1.1.1 Studying earthquakes

The beginnings of seismology were rooted in humanity's interests in earthquakes. The oldest seismoscope was invented by Zhang Heng of China's Han dynasty, in AD 132, which was called Houfeng Didong Yi (literally, "instrument for measuring the seasonal winds and the movements of the Earth"), shown in Figure 1 [2]. The description, says that it was a large bronze vessel, about 2 meters in diameter; at eight points around the top were dragon's heads holding bronze balls. When there was an earthquake, one of the mouths would open and drop its ball into a bronze toad at the base, making a sound and supposedly showing the direction of the earthquake. The available text says that inside the vessel was a central column that could move along eight tracks; this is thought to refer to a pendulum, though it is not known exactly how this was linked to a mechanism that would open only one dragon's mouth. The first ever earthquake recorded

by this seismograph was supposedly somewhere in the east. Days later, a rider from the east reported this earthquake [3].



Figure 1. Replica of Zhang Heng's seismoscope “Houfeng Didong Yi”

The beginning of modern seismic instrumentation dated back to 1895 in Japan where a horizontal pendulum based seismoscope was developed by John Milne [4] [5]. It had extremely low natural frequency allowing unprecedented resolution in measuring seismic vibrations. Until the nineteenth century, seismology mostly focused on the study of earthquakes. Analysis of the seismic wave propagation from the data obtained by seismometers and the development in understanding of the elastic wave theory enabled the understanding of the internal structure of the Earth. R. D. Oldham proposed a model of Earth with a liquid core by analyzing the travel time of long distance seismic waves through the Earth [4]. Andrija created crust-mantle boundary theory in 1909 [4], followed by a solid inner core theory by Lehmann in 1936 [6]. Thanks to the advancement in seismic instrumentation development, more and more new understandings of Earth's

internal structure were known by people. Nowadays, a number of seismometer networks are deployed to detect seismic events across the globe. By measuring the seismic waves emanating from a quake at different locations, the parameters of an earthquake can be determined, including hypocenter location, magnitude, event time, and etc. For instance, according to USGS, the 2011 Tōhoku earthquake, was a magnitude 9.0 (Mw) undersea earthquake off the coast of Japan that occurred on Friday, 11 March 2011 [7]. It was the most powerful known earthquake to have hit Japan, and one of the five most powerful earthquakes in the world overall since modern record-keeping began in 1900 [8]. The collection of this information over the years leads to advances in understanding the probability of earthquakes and also helps further study of the Earth's internal structure and the theory of plate tectonics.

1.1.1.2 Nuclear Monitoring

Seismology received a significant boost in 1950s and 1960s as a means to detect nuclear explosions [9]. Seismic monitoring is an important piece of the worldwide system dedicated to the detection of nuclear explosions and tests for the purpose of nuclear treaty monitoring. Nuclear nonproliferation is of the utmost importance to world peace, with the task being made increasingly more difficult due to the rising threat of non-state organizations gaining nuclear capability. Nuclear plant accident is another great concern all over the world. Although nuclear power plants are designed strictly to meet the nuclear energy safety standard, contrived mistakes, earthquakes or other natural disasters may cause nuclear accidents. Take the 2011 Tōhoku earthquake for example, in addition to loss of life and destruction of infrastructure, the tsunami triggered by the earthquake

caused a number of nuclear accidents, primarily the level 7 meltdowns at three reactors in the Fukushima I nuclear power plant complex, and the associated evacuation zones affecting hundreds of thousands of residents. To support next-generation nuclear monitoring, the National Nuclear Security Administration (NNSA) will need seismic sensors with new levels of sensitivity and deployability.

1.1.1.3 Planetary Exploration

National Aeronautics and Space Administration (NASA) is implementing its exploration agenda through plans to return to the Moon and develop a sustained human presence there. Establishment of structures suitable for human habitation on the Moon is a complex task in structural and environmental design. A lunar seismometer network should be a necessary precursor to human colonization for a number of reasons. The first is that the network can characterize the frequency, and location of moonquakes which can be used to make decisions about where to locate an outpost. Secondly, the seismometer can characterize the strength of a quake, which can be used as input for structural design requirements of lunar colonization architecture. Also, detailed knowledge of the lunar surface and subsurface structure through seismic research will be needed to ensure structural stability and survivability.

There are mainly three types of lunar seismic events: deep moonquakes, thermal moonquakes, and shallow moonquakes. Originating from depths of 700-1000 km, deep moonquakes often occur in nests and are the one of the most frequent identified sources of seismic activity [10]. The vast majority of the epicenters of deep moonquakes have been found on the near side of the moon due to the near side locations of the seismometer

stations and therefore it is not entirely certain that deep moonquakes originating on the far side have similar weak magnitudes. There is a need of seismic study to determine whether these quakes pose any threat to human colonization.

Thermal moonquakes are believed to be caused by diurnal temperature changes and are local, originating from nearby rock movement and fracturing or slumping of soil on lunar slopes. The magnitudes of these quakes are low but due to their proximity to the surface and efficiency, may release as much as 10^5 times more energy per year than deep moonquakes [11]. Lunar soil shear strength and thermally induced stresses are of the same order of magnitude [12], therefore these surficial quakes may be a result of slumping lunar soil. Seismic mapping of the frequency and location of these events may provide a vital tool for keeping astronauts safe while exploring crater walls and other locations where sudden slumping could be dangerous to any explorer.

Shallow moonquakes or high-frequency teleseismic events are much stronger than the previous mentioned quakes. The largest quake measured was a shallow moonquake of magnitude ~ 5.5 . For short term sortie missions, consideration of these quakes is less important, however, long-term colonization will no doubt experience a quake of this magnitude. This brings another topic for seismic study on the Moon: further mapping the spatial and temporal distribution events and providing a key input for a geographical location of a future outpost.

Our current knowledge of the seismic activity of the Moon is based solely on observations recorded by the Apollo Passive Seismic Experiment (PSE) network. Deployed during the Apollo 12, 14, 15 and 16 missions, it was limited to a triangular area on the lunar nearside with a baseline of only 1100 km. Each PSE consisted of a single

vertical sensor with a frequency range of 50 mHz to 10 Hz and three orthogonal sensors with a range of 4 mHz to 3 Hz. Although this network laid the foundation for our understanding of the internal structure of the Moon, there are many unanswered questions left. Does the Moon have a core? What is the exact vertical and horizontal stratification in the crust, mantle and core? What is the composition of the lunar interior? Are there stronger moonquakes than the recorded shallow moonquakes with magnitudes of 5 and more? Further open questions are summarized in a comprehensive list by Fagan [13] and Neal [14]. Significant advances in our understanding of the lunar interior inevitably require a new dataset collected by a long lived and global seismometer network.

Design of seismometers, especially for planetary exploration, is fraught with difficulties and compromises. Traditional wide-bandwidth spring-mass based seismometers are large, fragile, heavy, power-hungry, and, the most importantly require a lot of manpower. The devices are limited in size and mass and require more power primarily because achieving low thermal self-noise in such devices requires the use of large proof masses. On Earth, seismometers are installed by hand at a field site. This approach will not suffice for outer planets. One solution is to include seismic instrumentation on a penetrator, which would impact the planet at high speeds, embedding itself in the surface material. However, since penetrators experience an extreme deceleration as they land, any instrumentation they include must be able to withstand very high shocks. Furthermore, the seismicity of other planets is likely to be quite lower than it is on Earth – they are likely to be seismically “quiet”. Therefore, a low noise floor is required for an instrument to measure any seismic activity likely to be found on another planet. However, attempts to shrink the traditional designs using

MEMS fabrication processes have thus far met with limited success because of fragility and the inherent limitation of working mechanism of the solid-state mass-spring system, which still requires strict installation angle.

All the above demands demonstrate a tremendous need of developing physically small, light-weight, robust, low noise, high sensitivity, low power seismometers for Lunar exploration purposes. Also a mature and robust geophysical technology, will be used on Mars, as well, and will lay the foundation for further development and adaption for the use on other celestial bodies whose seismic activity is completely unknown.

1.1.2 State-of-Art Seismometers

Early seismometers consisted of a large stationary pendulum, with a stylus on the bottom. As the earth starts to move, the heavy mass of the pendulum has the inertia to stay still in the non-earth frame of reference. The result is that the stylus scratches a pattern corresponding with the Earth's movement. This type of strong motion seismometer recorded upon a smoked glass (glass with carbon soot). While not sensitive enough to detect distant earthquakes, this instrument could indicate the direction of the pressure waves and thus help find the epicenter of a local earthquake.

While early seismometers used optical levers or mechanical linkages to amplify the small motions involved, recording on soot-covered paper or photographic paper, modern instruments use spring-mass system and electronics. In early traditional systems, the weight is allowed to move, and its motion produces a voltage in a coil attached to the mass and moving through the magnetic field of a magnet attached to the frame. This type of seismometer is called electromagnetic or inductive seismometer and was first

developed by Prince Boris Galitzin in 1906 in Russia [5]. For years, inductive-type converters were the major type of instruments used in seismological measurement. For these sensors the low cut-off frequency is inversely proportional to the square root of the inertial mass. Also, heavy, multiple-turn coils are required to achieve higher gain and better resolution of weak signals. Both factors result in the fact that the size of the sensor is strongly dependent on the operating frequency range and resolution required. 10-Hz geophones are very small (10-30 G) and cheap, and have low gain (20 V/(m/s) typically). Short-period 1 Hz seismometers are very heavy (more than 10 kilos per component) and have gain (100-400 V/(m/s)) high enough to resolve very weak signals. A 1 Hz low-cut-off frequency is the practical limit for use of sensors of this type. Lower frequency would require extremely heavy and large devices. Attempts to move to lower frequencies using feedback was not very successful, with the fundamental reason being the low sensitivity of the inductive converter at low frequencies: this type of the converter produces a response proportional to the velocity of the moving mass, which is small below the natural frequency of the sensor mechanical system.

Great progress in seismological instrumentation has been achieved in the last few decades, to a significant extent, as a result of the substitution of capacitive for inductive converters and the introduction of feedback. In these systems, the mass is held nearly motionless relative to the frame by an electronic negative feedback loop. The displacement of the mass relative to the frame is measured by a capacitive displacement sensor, and a feedback loop including a force transducer generates a magnetic force to balance the external force to keep the mass nearly motionless. The current needed to produce this force is the output of the seismometer. By measuring the current, we have a

measure proportional to the external acceleration. This type of sensor is also called a force balance accelerometer (FBA). The FBA design is widely used in velocity broadband seismometers which created a new age in seismic instrumentation. Development of the broadband seismometer started by Wielandt and Streckeisen in 1983 [5]. The broadband seismometer can record ground motion over a large range of periods by introducing a feedback system that extends the response to very long periods (over 200 seconds). Some of the commercialized state-of-art seismometers are shown in Figure 2. STS-2 (Figure 2(a)) is a three-axis seismometer by Streckeisen which has a mechanical time period of 120 second [15]. CMG-40T (Figure 2(b)) and CMG-3T (Figure 2(c)) are Güralp's three component seismometers [16]. Table 1 summarizes some of the state-of-art seismometers from different vendors with comparisons in various parameters.

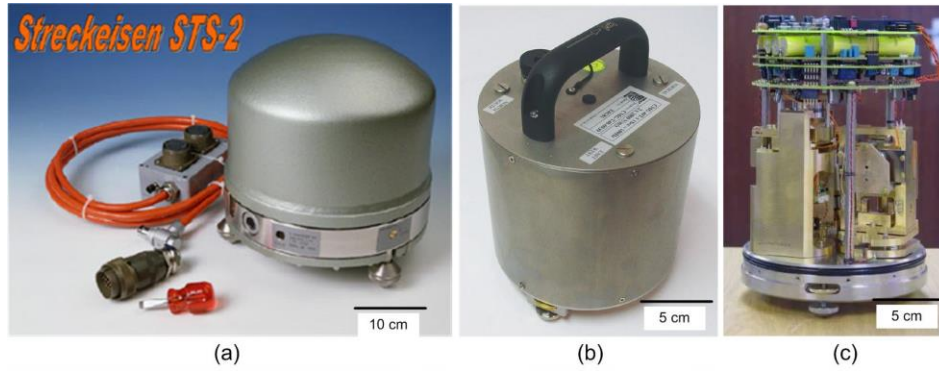


Figure 2. Commercialized state-of-art seismometers.

Table 1. Parameters of state-of-art solid-state mass-spring based seismometers

Model	Size (cm)	Self-noise (m/s ² /Hz ^{1/2})	Natural frequency	Proof mass
Streckeisen STS-2	$\varnothing 23 \times 26$	3.16×10^{-11}	120 sec	14 kg
Güralp CMG-3T	$\varnothing 17 \times 38$	1.78×10^{-10}	120 sec	14 kg
Güralp CMG-40T	$\varnothing 15 \times 20$	1.78×10^{-9}	30 sec	7 kg
Nanometrics Trillium 120P	$\varnothing 22 \times 18$	5.62×10^{-10}	30 sec	11 kg
Geotech S-13	$\varnothing 17 \times 38$	4.47×10^{-10}	1 Hz	5 kg
Kinometrics SS-1	$\varnothing 14 \times 35$	4.98×10^{-10}	1 Hz	1.45 kg

MEMS capacitive micro-accelerometers, based on solid-state mass-spring system, have been developed for more than a decade [17, 18, 19, 20, 21, 22, 23] and commercialized [24-25] for the automobile industry and consumer electronics. Furthermore, MEMS researchers are improving the accelerometers' performances to reach planetary seismic research requirements, i.e. high resolution, low noise floor, and wide dynamic range [1]. In short, capacitive converters are sensitive to the inertial mass displacement (rather than the velocity as is the case with inductive converters), which results in radically higher and flat sensitivity response in the low-frequency portion of the spectrum. Feedback stabilized the parameters, extended the pass band and increased the instrument dynamic range.

1.2 MEMS Capacitive Accelerometers

Motion sensors, including accelerometers and gyroscopes, provide measurement of movement in at least six degrees of freedom. The simplest way to do motion sensing is with a solid-state mass-spring system, creating a damped simple harmonic oscillator. The movement of the solid-state proof mass can be measured with respect to displacement, velocity, or acceleration by suitable mechanical-electrical transducers. Efforts to

miniaturize linear accelerometers and gyroscopes for inertial systems are mostly concentrated around MEMS technology. Similarly in terms of design, fabrication, and readout, accelerometers and gyroscopes are the current leaders in commercially successful MEMS technology. Among a variety of transduction mechanisms underlying solid-state MEMS motion sensors, the most successful types are based on capacitive transduction due to the simplicity of the sensor element itself, easy to integrate with modern electronic systems, no need for exotic materials, low power consumption, and good stability with respect to temperature. Although capacitive transducers have a characteristic nonlinear capacitance vs. displacement response, feedback is commonly used to convert the signal to a linear output.

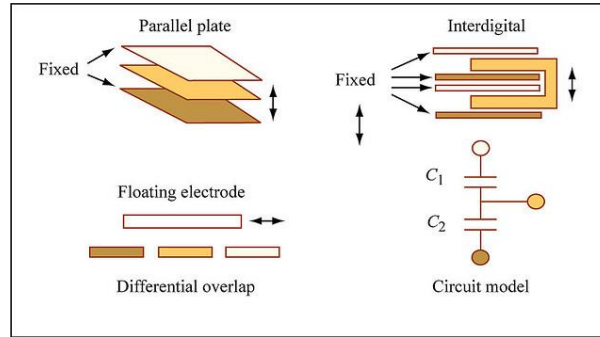


Figure 3. Different types of differential capacitors.

In a MEMS capacitive accelerometer, differential capacitors are used as position sensor to sense the relative displacement of the proof-mass to the reference frame. There are mainly three types of differential capacitors as shown in Figure 3 [26]. In all three examples, there are three electrodes used for the measurement, with two capacitance C_1 and C_2 equal value when the moveable component is centered. Motion of the moveable

component in the indicated direction increases one capacitance and decreases the other. Take the parallel-plate example, with the gap of the upper capacitor G_1 and that of the lower capacitor G_2 , and equal area of both capacitors. If a voltage of $+V_s$ is applied to the upper plate, and a voltage of $-V_s$ is applied to the lower plate simultaneously. The output voltage is

$$V_o = -V_s + \frac{C_1}{C_1 + C_2} (2V_s) = \frac{C_1 - C_2}{C_1 + C_2} V_s \quad (1)$$

Since the areas of C_1 and C_2 are equal,

$$V_o = \frac{G_2 - G_1}{G_1 + G_2} V_s \quad (2)$$

Figure 4 shows the schematic and SEM (scanning electron microscopy) pictures of the sensing part of a MEMS capacitive accelerometer (ADXL150, Analog Devices) [27]. The shuttle forms the proof mass. It is suspended on folded springs that are attached to the substrate only at certain anchor points. Cantilevered electrodes are attached to the proof mass. Each cantilever electrode is positioned between two fixed electrodes, forming a lateral differential capacitor of the inter-digital type shown in Figure 3.

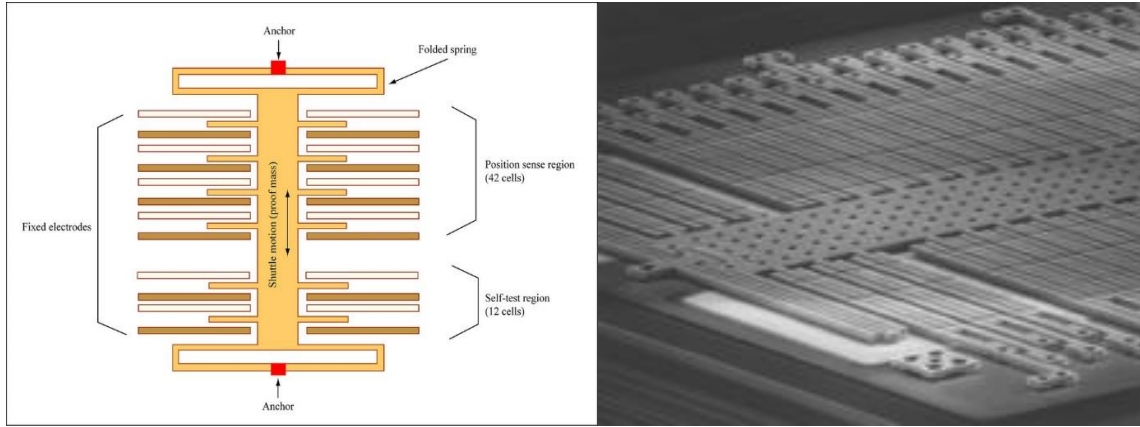


Figure 4. Sensing element of commercialized ADXL150 MEMS capacitive accelerometer.

The block diagram of ADXL series accelerometer is shown in Figure 5. This is a close-loop system with a force-feedback which benefits the linearity and accuracy of the system. Comparing with the open-loop system design, sacrifice sensitivity in a tolerance interval and increase the dynamic working bandwidth.

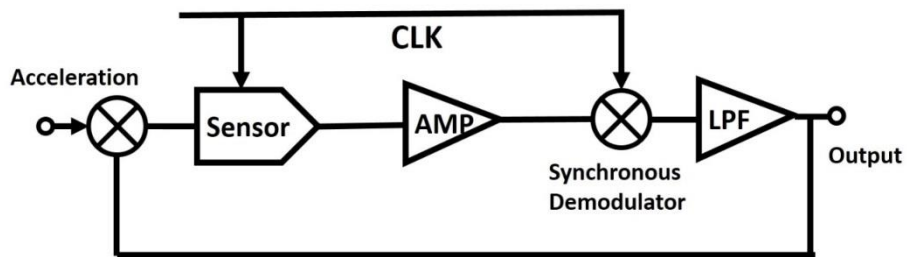


Figure 5. Block diagram of ADXL series accelerometer.

Table 2 compares the specifications of previously reported MEMS capacitive accelerometers including devices from research groups and commercialized products.

Table 2. Comparisons of MEMS capacitive accelerometers from research groups and commercialized products

	Lemkin [17]	Tseng [19]	Qu [22]	Sun [23]
Sensing range (G)	± 1.4	± 6	± 3.2	± 6
Power dissipation (mW)	45	0.7	1	5
Sensitivity (mV/G)	N/A	191	520	0.53
Noise floor ($\mu\text{G Hz}^{-1/2}$)	110	354	12	120×10^3
Resonant frequency (kHz)	3.9	4.4	3.23	8.49
	Wu [20]	Chae [21]	Freescall (MMA6361L) [24]	ADI (ADXL203) [25]
Sensing range (G)	± 6	± 1	± 6	± 1.7
Power dissipation (mW)	30	N/A	1.3	2.1
Sensitivity (mV/G)	130	490	206	1000
Noise floor ($\mu\text{G Hz}^{-1/2}$)	50	1.6	350	110
Resonant frequency (kHz)	5.8	>0.6	6.0	5.5

Although MEMS capacitive accelerometers in combination with other sensors, such as compass, pressure sensor, and GPS, have created a consumer electronics sensing package that works as the intelligent interface for users to interact with their electronics and, further on, with external environments, and have reasonable performance with low cost CMOS-compatible silicon microfabrication technology, there are huge markets for micro accelerometers with applications designed for military inertial navigation/guidance and high-resolution seismic sensing for planetary exploration, which require high sensitivity, low noise in low frequency range.

There are a number of research groups aiming to develop micro seismometers capable of being used in extraterrestrial exploration based on solid-state mass-spring system using MEMS fabrication techniques [28]. The main goal of these research efforts is to reduce the overall size of the system while maintaining adequate sensitivity and low

noise. Often accompanying a reduction in instrument size is a decrease in proof mass and power. However, the difficulty in developing micro-seismometers using a solid-state mass-spring system is the compromises between size (proof mass) and performances (sensitivity, noise and dynamic range). The proof mass of a micro seismometer developed by MEMS technology is limited to a very small value. Due to the reduction in proof mass, the resonant frequency of MEMS accelerometers is usually in the kilo Hz range (Table 2), thus the sensitivity at low frequencies becomes relatively weak. Also, for small proof mass, Brownian motion becomes a big issue. The random thermal motion of proof-mass molecules or surrounding gas molecules can cause the proof-mass to change position instantaneously. This instantaneous motion is picked up by the position sensors and increases the noise floor. Furthermore, reduction in the proof-mass size limits the dynamic range in measuring at longer periods. For longer periods with small proof mass, the spring needs to be soft, which will produce bigger movement at high seismic energy. The compact framework of the miniature seismometer will not allow a large range of motion, therefore, degrading the dynamic range.

Despite of the above difficulties of fabricating micro seismometers, MEMS researchers have tried all means to minimize the limitations to the extent possible. Low-noise lateral suspension based on Parylene was demonstrated by Suzuki et al [29] which shows the advantage of using polymer to build very low resonant frequency suspensions. Although the mass of a MEMS accelerometer is substantially lower than the conventional seismometers, deep reactive ion etching (DRIE) which is one of recent MEMS techniques enables high aspect ratio structure which allows significant increase in proof mass, thus decrease in resonant frequency and noise. By increasing the proof mass using

DRIE and improving the suspensions, Pike has developed a micro seismometer based on MEMS capacitive accelerometer, which has the potential for planetary missions [30] [31]. Their prototype has a resonant frequency of 10 Hz, and achieves $4.0 \text{ nG/Hz}^{-1/2}$ self-noise. It also has high out-of-plane stiffness and low cross-axis sensitivity. Magnetic force feedback is used to improve the dynamic range and the device drift. Figure 6 shows their packaged micro seismometer.

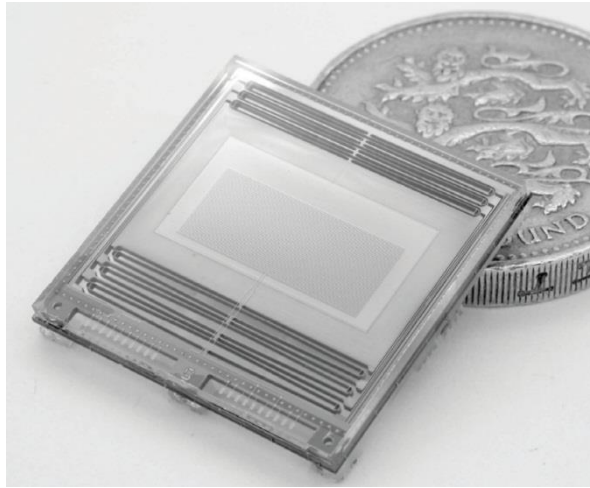


Figure 6. The packaged micro seismometer by Pike, et al [31]

1.3 Basic Working Principles of The Mass-spring System in Seismometers

Since the ground motion measurements are done in a moving reference, almost all seismometers are based on mass-spring system, where the inertia of the suspended mass will tend to remain stationary in response to external motion. The relative motion between the suspended proof mass and the ground will then be a function of the ground's motion. Figure 7 shows a simplest schematic of mass-spring system in a seismometer that

can detect vertical ground motion. It consists of a proof mass suspended from a spring and a damper.

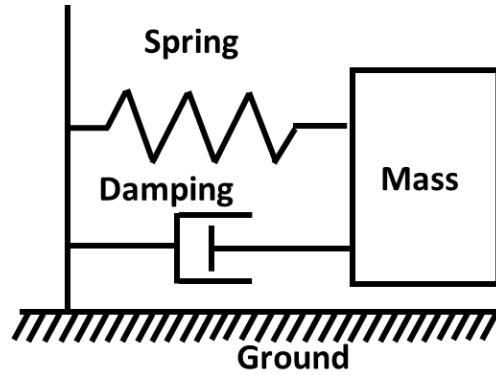


Figure 7. A schematic of an inertial seismometer based on mass-spring damper.

1.3.1 Frequency Response

Let $u(t)$ be the ground's vertical motion and $z(t)$ the displacement of the liquid inertial mass m relative to the ground, both positive upwards. There are two real forces acting on the mass:

- Spring force, $-kz$, where k is the spring constant, negative because the spring opposes the mass displacement.
- Damping force, $-d\dot{z}$, where d is the damping constant, negative since it also opposes the motion.

The acceleration of the mass relative to an inertial reference frame will be the sum of the acceleration with respect to the ground \ddot{z} and the ground acceleration \ddot{u} . According to Newton's law, the sum of forces must be equal to the mass (m) times the acceleration, we have

$$-kz - d\dot{z} = m\ddot{z} + m\ddot{u} \quad (3)$$

Given the resonant angular frequency $\omega_0 = \sqrt{k/m}$, and damping ratio $h = d/2m\omega_0$,

Equation (3) can be written as

$$\ddot{z} + 2h\omega_0\dot{z} + \omega_0^2 z = -\ddot{u} \quad (4)$$

This equation shows that the ground acceleration can be obtained by measuring the relative displacement of the mass, z , and its time derivatives. It is not easy to solve directly the output signal for any arbitrary input signal. However, since an arbitrary signal can be described as a superposition of harmonics, the simplest way to solve Equation (4) is to assume an input of a harmonic ground motion and solve for the solution in frequency domain. Set the ground motion as

$$u(t) = U(\omega)e^{j\omega t} \quad (5)$$

where $U(\omega)$ is the complex amplitude and ω is the angular frequency. Since a seismometer can be assumed to represent a linear system, the mass relative motion is also a harmonic motion with the same frequency.

$$z(t) = Z(\omega)e^{j\omega t} \quad (6)$$

So we have

$$\ddot{u} = -\omega^2 U(\omega)e^{j\omega t} = a(\omega)e^{j\omega t} \quad (7)$$

$$\dot{z} = i\omega Z(\omega)e^{j\omega t} = V(\omega)e^{j\omega t} \quad (8)$$

$$\ddot{z} = -\omega^2 Z(\omega)e^{j\omega t} = A(\omega)e^{j\omega t} \quad (9)$$

Inserting Equation (7)-(9) to Equation (4), and dividing by the common factor $e^{j\omega t}$, we can obtain the relationship between the output and the input signal in frequency domain.

Almost all traditional seismometers are inductive type seismometers which have fixed coil and a magnet moving with the mass. The output voltage from the coil is proportional to the velocity of the mass relative to the frame. This kind of electromagnetic seismometer is also called velocity transducer. The acceleration, velocity and displacement response for the velocity transducer are

$$T_a^v(\omega) = \frac{V(\omega)}{a(\omega)} G = \frac{-i\omega G}{\omega_0^2 - \omega^2 + i2\omega\omega_0 h} \quad (10)$$

$$T_v^v(\omega) = \frac{V(\omega)}{v(\omega)} G = \frac{\omega^2 G}{\omega_0^2 - \omega^2 + i2\omega\omega_0 h} \quad (11)$$

$$T_d^v(\omega) = \frac{V(\omega)}{U(\omega)} G = \frac{-i\omega^3 G}{\omega_0^2 - \omega^2 + i2\omega\omega_0 h} \quad (12)$$

where G is the generator constant which relates the velocity of the mass (relative to the frame) to the output voltage of the coil, in the unit of V/(m/s).

Mechanical seismometers directly measure the relative displacement of the proof mass. For the VBB seismometers with FBA system and MEMS accelerometers, the output of capacitive transducers is in proportional to the displacement of the proof mass relative to the reference frame. The acceleration, velocity and displacement frequency response of the capacitive transducer are

$$T_a^c(\omega) = \frac{Z(\omega)}{a(\omega)} D = \frac{-D}{\omega_0^2 - \omega^2 + i2\omega\omega_0 h} \quad (13)$$

$$T_v^c(\omega) = \frac{Z(\omega)}{v(\omega)} G = \frac{-i\omega D}{\omega_0^2 - \omega^2 + i2\omega\omega_0 h} \quad (14)$$

$$T_d^c(\omega) = \frac{Z(\omega)}{U(\omega)} G = \frac{\omega^2 D}{\omega_0^2 - \omega^2 + i2\omega\omega_0 h} \quad (15)$$

where D is the sensitivity of the capacitive transducer in the unit of V/m.

Figure 8 shows the schematic curves of amplitude frequency responses to input displacement, velocity and acceleration, for a 1 Hz inductive type seismometer and a 1 Hz mechanical seismometer (or capacitive transducer output in a 1 Hz VBB seismometer). The axes are logarithmic and the asymptotic slope for each segment is indicated [1].

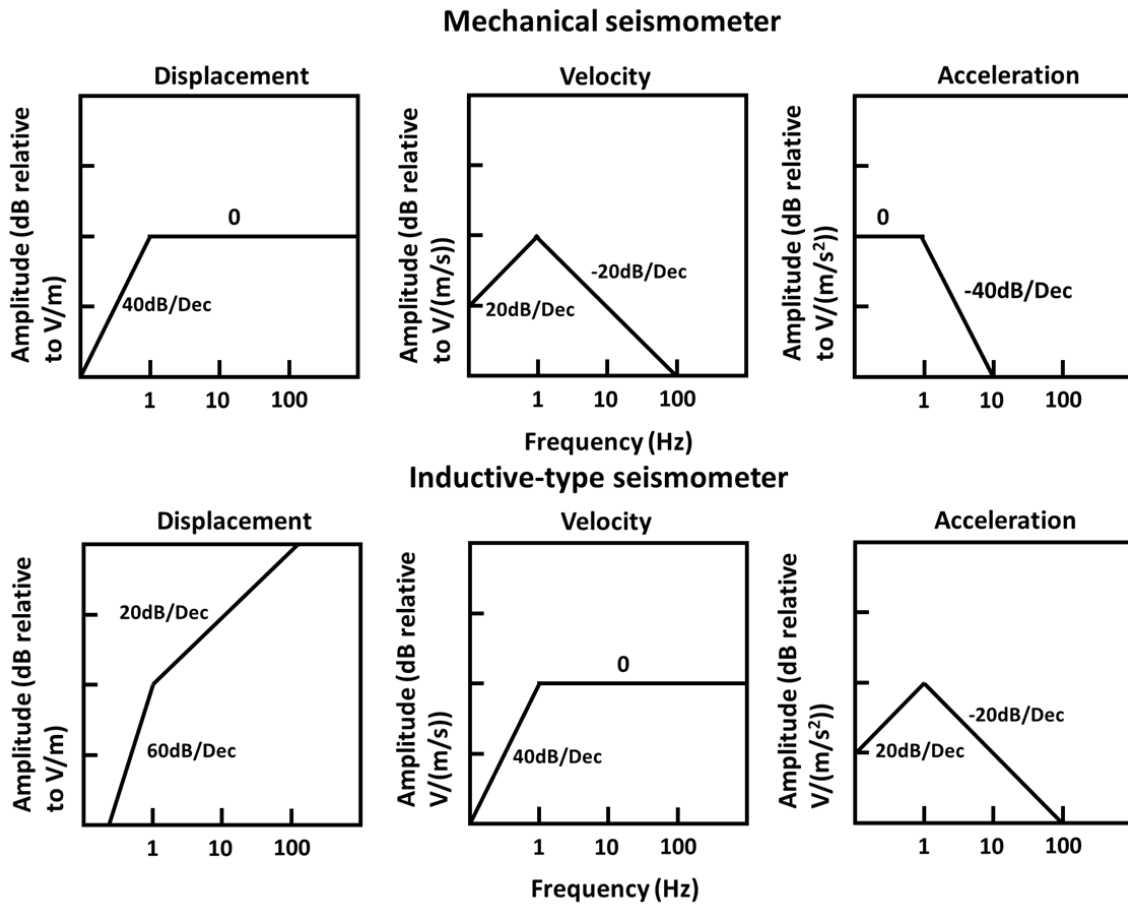


Figure.8 Schematic of amplitude frequency responses for input displacement, velocity and acceleration, for a 1 Hz inductive type seismometer (velocity transducer, top), and for a 1 Hz mechanical seismometer or the output of capacitive transducer in a 1 Hz VBB seismometer (bottom).

1.3.2 Noise

One of the key requirements of seismometer is to make it sensitive enough to detect the smallest seismic signals, given that noise sets a limit to the level of detection. The instrument noise is due to both the electronic noise and the mechanical noise of the mass-spring system. The electronic noise is generally well quantified for the amplifiers and the feedback circuit. The fundamental limit to the mechanical self-noise is set by the Brownian motion of gas molecules hitting the proof mass. Usher [32] shows the noise-equivalent acceleration (NEA) for a unit bandwidth at any frequency is given by

$$NEA^2 = 4k_B T \frac{\omega_0}{mQ} \quad (16)$$

where k_B is the Boltzmann constant, T is the temperature in Kelvin, Q is the quality factor which measures the energy loss versus energy stored per cycle for a mass-spring system. NEA is expressed in the unit of $m/s^2/\sqrt{Hz}$. Seismometers with very large mass, high Q and extremely long period have lower mechanical self-noise. For miniaturized seismometers and MEMS seismometers, the proof mass decreases with miniaturization and therefore it is harder for the device to have low resonant frequency. STS-2 and CMG-3T have ~ 14 kg proof-mass and a long period of 120 seconds, so they have NEA less than $10^{-10} m/s^2/\sqrt{Hz}$. Oyo-Geospace HS-1 [33] with much lower mass of 22.7 g and resonant frequency of 4.5 Hz have higher self-noise of $1.07 \times 10^{-8} m/s^2/\sqrt{Hz}$.

CHAPTER 2

MOTION SENSORS BASED ON MOLECULAR ELECTRONIC TRANSDUCER

As opposed to a solid inertial mass, a molecular electronic transducer is sensitive to the movement of a liquid electrolyte relative to fixed electrodes. METs are part of a third class of fundamental electronic devices, characterized by charge transfer via ions in solution—hence the name “Solion”. This is in contrast to solid-state electronics (charge transfer by electron/hole pairs in a solid conductor or semiconductor) and vacuum tubes (charge transfer by free electrons in an ionized gas or vacuum). Solion technology was first developed in the 1950s by US-Navy sponsored research. Early applications of Solion devices were for detection of low-frequency acoustic waves, either in the form of an infrasonic microphone or limited-band seismometer [34, 35, 36, 37]. Significant work on Solion motion detectors was continued in Russia, where the term “Molecular Electronic Transducer” was introduced to describe such a device [38]. Inspired by the exceptionally high rate of mechanical signal conversion to electric current in MET involving mass and charge transport, pioneering MET studies [39, 40, 41, 42, 43, 44, 45] provide an alternative paradigm in the development of motion sensors in wide variety of applications including nuclear explosion monitoring and seismic sensing in planetary exploration [46, 47, 48]. The advantages of MET motion sensors include their small size, lack of fragile moving parts (thus high shock tolerance), high sensitivity and low noise especially at low frequencies, and independence of the response on installation angle.

2.1 Molecular Electronic Transducer-Principle of Operation

Figure 9 illustrates the basic concept of a MET sensing element, consisting of an electrochemical cell with two anode-cathode pairs. An electrolyte-filled channel allows the electrolyte to move inertially along the channel's length. Four electrodes configured as anode-cathode-cathode-anode (ACCA) separated by dielectric layers span the width of this channel. Holes through the electrodes allow the flow of electrolyte. Each anode-cathode pair is an electrochemical cell, in which charges are transferred between anode and cathode by ions in the electrolyte. Traditionally, standard machined platinum (Pt) mesh is used to make the electrodes, and plastic or ceramic grids produce the dielectric inter-electrode spacers [49]. This approach is convenient to quickly produce samples, but significantly limits the possible range of the geometrical parameters of the cell and consequently the optimization possibilities of the sensing cell. Meanwhile making sizes of elements of the cell smaller expands the frequency range and decreases convection produced noise inside the sensitive cell. An alternative approach to build the sensing element is to use MEMS techniques, which have reduced the internal dimensions of MET electrodes close to 1 μm , improved the sensitivity and reproducibility [48].

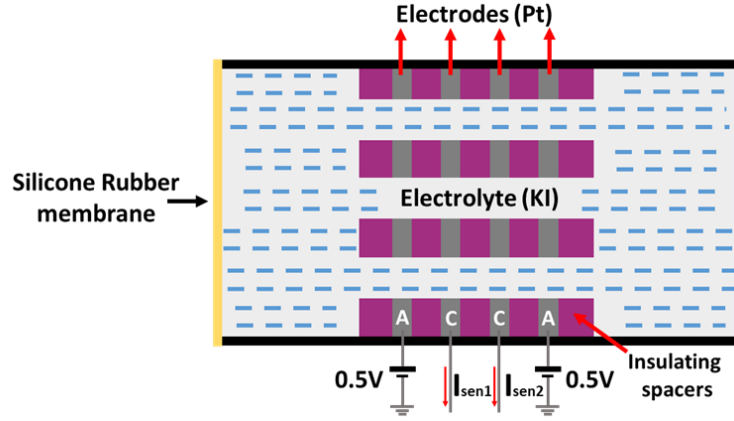


Figure 9. Schematic of the basic MET sensing element.

The sensing mechanism of the MET is based on using of the electrochemical cell where reversible chemical reactions transfer charge between anode and cathode via electrolyte ions in solution. Typically, MET uses concentrated iodine-iodide electrolyte containing potassium iodide (KI) or lithium iodide (LiI) and a small amount of elemental Iodine (I_2) [50]. In the presence of iodide, iodine turns into a soluble compound, tri-iodide, as follows [50]:



when the electrodes are biased and thus current passes through the electrochemical cell, the following reversible active electrochemical reactions occur on the electrodes:

On cathodes, reduction of tri-iodide:



The reverse reaction takes place on anodes:



The electrical current through the solid/liquid interface becomes possible because of the tri-iodide ions presence in the solution. That's why this component of the solution is called active. According to Equation (16) and (17), the interface charge transfer is associated with generation and absorption of the tri-iodide ions on the electrode surface. So the electrical current through any electrode can be related to the flux of active ions toward or backward of the electrode according to the following:

$$I = Dq \left(\oint_S (\nabla c, \mathbf{n}) dS \right) \quad (20)$$

where D is the diffusion coefficient, c is the concentration of the active charge carriers, q is the charge transferred across the interface in single electrochemical reaction (two times absolute values of the electron charge in our case), \mathbf{n} is a unit vector normal to the surface of the electrode, integration is done over S , electrode surface area. Here only diffusion is considered as mechanism responsible for the active ions transport in the electrolyte volume. The migration is not included due to the screening of the electrical field in the highly concentrated electrolyte and the convection does not contribute to charge transfer through the electrode surface due to zero-velocity condition on the solid surface.

The operation principle of MET can be described as follows: when electric voltage is applied to the system, electrochemical current (background current) appears, regardless of the presence of mechanical motion of the electrolyte. As the inter-electrode voltage is increased, the reaction rates on the electrodes increase too. Finally, in the situation when any tri-iodide ion arrives the cathode immediately participates in the electrochemical reaction in Equation (16), further increase of the voltage does not change

the current and the saturation regime occurs. In this regime the cathode current is sensitive to variation of volumetric transport of tri-iodide ions. Anode current variations follow the cathode ones, keeping the electrolyte uncharged. When there is no external acceleration, a symmetric pattern of tri-iodide ion concentration with its gradient develops as shown in Figure 10 (a). So the output of the sensor which is the differential cathodes' current determined by the tri-iodide ion concentration gradient near the two cathodes will be zero.

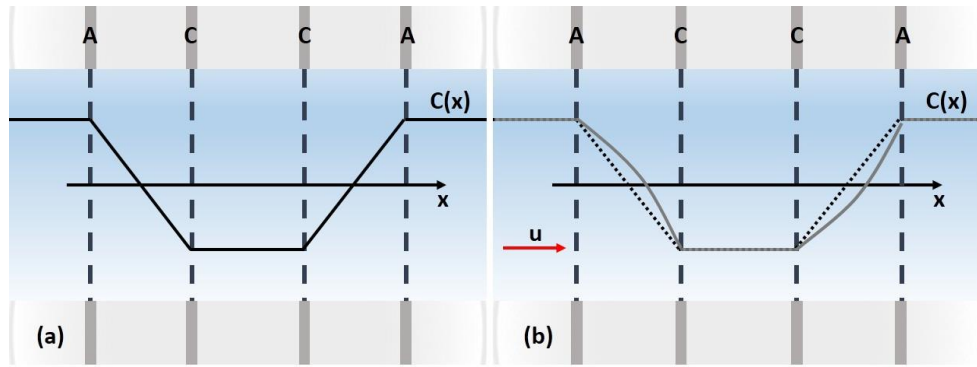


Figure 10. Tri-iodide ion concentration with its gradient for a MET motion sensor. (a) No external acceleration, (b) In the presence of external acceleration.

In the presence of a mechanical motion input, electrolyte starts moving due to inertia, and convective transport of ions changes the electrode current according to the mechanism described above. An unsymmetrical pattern of tri-iodide ion concentration with its gradient develops as shown in Figure 10 (b). There are opposite changes in the tri-iodide concentration gradient near the two cathodes. Therefore, the difference of the cathode currents in two anode-cathode pairs which is employed as the output signal for a MET motion sensor will no longer be zero. Although each electrode current is non-linear

with respect to fluid velocity, the combined output of both cathodes is linear for a very wide range of fluid velocities. Mathematically, the sensor's output current is given by [50]:

$$I_{out} = I_{C2} - I_{C1} = Dq \left(\oint_{S_{C2}} (\nabla c, \mathbf{n}) dS_{C2} - \oint_{S_{C1}} (\nabla c, \mathbf{n}) dS_{C1} \right) \quad (21)$$

where I_{C1} , I_{C2} are the currents through the surface of the corresponding cathodes, S_{C1} , S_{C2} are the surface areas of the corresponding cathodes.

2.2. Transfer Function

A signal conversion in MET motion sensor can be considered as a superposition of two processes: first, input motion is converted to fluid motion of the electrolyte by mechanical system. Next, the electrolyte's velocity is measured by the electrochemical system, resulting in an output current of the sensor. Therefore, the frequency-dependent transfer function of the entire device can be written as:

$$H(\omega) = H_{mech}(\omega)H_{ec}(\omega) \quad (22)$$

where $H_{mech}(\omega)$ describes the mechanical response of the fluidic system, which in the case of linear MET sensor, is analogous to a solid-state damped, driven harmonic oscillator. In this sense, the restoring force to the liquid inertial mass is provided by the rubber membranes which are located at the two ends of the channel to seal the electrolyte, and the damping force is caused by hydrodynamic resistance of the electrolyte as it flows through the sensing element. The equation that governs motion of the electrolyte can therefore be expressed as:

$$\frac{d^2V}{dt^2} + \frac{R_h S_{ch}}{\rho L} \frac{dV}{dt} + \frac{k}{\rho L} V = -S_{ch} a \quad (23)$$

where V is the volume of fluid passing through the channel, a is the external acceleration, R_h is the hydrodynamic resistance which is solely determined by the channel geometry in laminar flow condition, k is the coefficient of volume stiffness and depends only on the characteristics of the membrane, ρ is the density of the electrolyte, S_{ch} is the cross-section area of the channel and L represents the length of the channel, filled with electrolyte. By transforming Equation (21) to the frequency domain, the magnitude of the transfer function of the fluid mechanical motion in frequency domain can be obtained as follows:

$$|H_{mech}(\omega)| = \left| \frac{Q(\omega)}{a(\omega)} \right| = \frac{\rho L}{\sqrt{\left(\frac{\rho L}{S_{ch}}\right)^2 \frac{(\omega^2 - \omega_0^2)^2}{\omega^2} + R_h^2}} \quad (24)$$

where $Q(t) = dV(t)/dt$ is the volumetric flow rate.

$H_{ec}(\omega)$ in Equation (22) describes the ability of the electrochemical system to detect electrolyte motion as a function of frequency. A simple model for $H_{ec}(\omega)$ was derived analytically by Larcam [7], having a form of:

$$|H_{ec}(\omega)| = \left| \frac{I(\omega)}{Q(\omega)} \right| = \frac{C}{\sqrt{1 + \left(\frac{\omega}{\omega_D}\right)^2}} \quad (25)$$

where C ($A/(m^3/s)$) is the conversion factor of the electrochemical cell, $\omega_D = D/d^2$ is the diffusion frequency and d is the inter-electrode distance. In-depth characterization of the above electrochemical subsystem is based on the analytical and numerical solution of the following partial differential equations [41, 45, 51, 52, 53, 54]:

$$\rho \left(\frac{\partial \mathbf{u}}{\partial t} + (\mathbf{u} \cdot \nabla) \mathbf{u} \right) = -\nabla P + \mu \nabla^2 \mathbf{u} \quad (26.1)$$

$$\nabla \cdot \mathbf{u} = 0 \quad (26.2)$$

$$\frac{\partial c}{\partial t} + \nabla \cdot (-D \nabla c + c \mathbf{u}) = 0 \quad (26.3)$$

Equation (26.1) is the time domain Navier-Stokes equation describing momentum balances, where ρ denotes the density (kg/m^3), \mathbf{u} is the velocity (m/s), μ denotes dynamic viscosity ($Pa \cdot s$), and P equals pressure (Pa). Equation (26.2) is the continuity equation for incompressible flow. The boundary conditions include a known pressure difference which drives the flow through the channel and the velocity is zero at the wall. Equation (26.3) is the diffusion-convection Nernst-Planck equation showing the tri-iodide transport balance. Usually, on cathodes, zero concentration condition is used, which corresponds to the saturation current regime described above. Dielectric surfaces are considered as non-penetrable for the ions (zero flow condition). For anodes, fixed concentration condition is frequently used, although this sort of condition can't be considered as well-founded. The problem of the correct formulation of the boundary condition on anode is discussed in [54]. Fortunately, the boundary condition on anodes has little effect on cathodes currents difference which is used as the system output signal.

Several theoretical analyses have been conducted on the electrochemical system frequency response at both low and high frequencies [41, 51, 52]. At low frequencies, where diffusion length $\lambda_d = \sqrt{D/\omega}$ appears to be much higher than the characteristic dimension which is the inter-electrode spacing d of the four-electrode structure:

$$I \xrightarrow{\omega \rightarrow 0} Q \cdot \text{const} \quad (27)$$

Therefore, using Equation (22):

$$H(\omega) \xrightarrow{\omega \rightarrow 0} \text{const} \cdot \omega \quad (28)$$

As frequency increases, the sensitivity starts to decay as λ_d becomes lower than the characteristic dimension of the electrode system d . For the mesh electrodes made with cylindrical wires, and $\omega \gg D/d^2$, the amplitude of cathode current yields:

$$I \xrightarrow{\omega \gg D/d^2} Q \cdot \omega^{-3/2} \quad (29)$$

Therefore, using Equation (8):

$$H(\omega) \xrightarrow{\omega \gg D/d^2} \text{const} \cdot \omega^{-5/2} \quad (30)$$

2.3. Feedback Subsystem

The feedback subsystem is added to allow an additional controllable force to act on the mechanical system. The feedback system herein introduces a layer of complexity into the overall system's transfer function. The simplified block diagram shown as Figure 11 illustrates how the input signal is manipulated by each subsystem. Text in blue describes the physical parameters being affected or measured in each step. The input signal is processed by the mechanical and electrochemical systems in order to produce the output signal, which is in turn used to adjust the mechanical system by the feedback system. The feedback current I_{FB} is simply the output current modified by a feedback parameter F . Finally, the effect of the feedback is applying to the inertial mass with additional counterforce, opposite to inertial force, and consequently effectively decreasing the input acceleration. In the feedback system described above, a higher output signal gives negative feedback impeding fluid flow, thereby increasing the

dynamic range of measurable signals. Moreover, this could be used to adjust sensitivity frequency response, allowing desired signals in certain bandwidth.

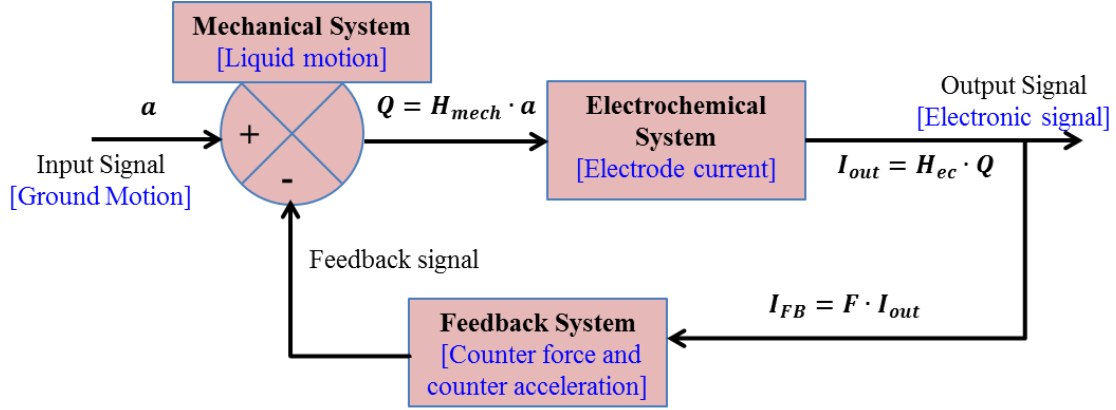


Figure 11. A block diagram of MET motion sensor including feedback subsystem.

2.4. Noise

The main contributors to the self-noise of the MET sensor are the thermo-hydrodynamic self-noise, convection-induced self-noise, and geometry noise [40, 55].

2.4.1. Thermohydrodynamic Self-Noise

The thermohydrodynamic self-noise is generated from the fluctuations of the pressure difference on both sides of the channel of MET sensor. In units of input acceleration, this noise spectral density is frequency independent:

$$\langle a \rangle_{\omega}^2 = \frac{2k_B \cdot T \cdot R_h}{\rho^2 L^2} \quad (31)$$

where T is the absolute temperature, k_B is Boltzmann's constant, ρ is the electrolyte density, L is the length of the transducer channel, R_h is the hydrodynamic impedance of the transducer which is given by:

$$R_h = \frac{8\mu l}{\pi r^4} \quad (32)$$

where r is the radius of the circular cross-section of the channel, l is the sensing element length and μ is the viscosity of the fluid. It can be seen that the lower R_h , higher ρ and L result in lower thermohydrodynamic self-noise. For a typical MET sensor with $R_h = 5 \times 10^8 (\text{N} \cdot \text{s})/\text{m}^5$ and $L = 5 \times 10^{-2} \text{ m}$, the theoretical thermohydrodynamic self-noise is $3 \text{ nG}/\sqrt{\text{Hz}}$.

2.4.2. Convection-Induced Self-Noise

The convection-induced self-noise is the result of the natural convection of the liquid [55]. Even if the liquid as a whole is stable, small local variations of the liquid density produce flows in the liquid. These flows generate an additional noise in the MET cell output current. This process is difficult to describe analytically. However, numerical modeling and experimental results can provide enough data to calculate the convection self-noise and can be used to predict its value for any specific configuration of the MET cell. In general, the value of the convection induced self-noise depends on the Rayleigh number (Ra) of the electrolyte. It has been proven both experimentally and numerically that the convection self-noise decreases as Ra decreases. Lower Ra corresponds to a lower electrolyte concentration and smaller typical dimensions of the elements of the transducer cell. On the other hand, Ra cannot be too small because that would correspond

to a very small size for the transducer cell and very small concentration of the electrolyte, which usually means high hydrodynamic impedance (high thermohydrodynamic noise) and low sensitivity of the transducer, respectively.

2.4.3. Geometry Self-Noise

The geometry self-noise is proportional to the electrochemical part of the transfer function of MET transducer. To calculate the geometry self-noise, the following equation can be used:

$$\langle v \rangle_f^2 = \beta \frac{4k_B T}{R_h} \overline{k_f}^2 \alpha^2 \quad (33)$$

where $\overline{k_f}$ is the averaged electrochemical part of the transfer function, α is the transducer conversion coefficient from output noise current to input noise velocities, and β is an empirical coefficient. The geometry noise is the dominant one at very low frequency.

2.4.4. Shot Noise

The shot noise of the MET sensor is given by the following formula:

$$\langle v^2 \rangle_f = \frac{2qI}{K} \quad (34)$$

where I is the quiescent current passing through the cell, K is the transducer conversion coefficient, q is the absolute value of the charge passing through the electrode boundary in the elementary chemical reaction on the electrode. In the electrochemical system usually used in MET transducer, q equals $2e$, where e is the absolute value of the charge of the electron.

2.4.5. Electronic Self-Noise

Electronic self-noise of MET sensor comes from the signal conditioning electronics, including the current to voltage converter and filters. The filters have unity gain in the proposed instrument pass band and do not contribute to the electronic self-noise. The equivalent input-referred electronic noise can be written as follows:

$$\langle v^2 \rangle_f = \frac{I_f^2 + U_f^2 \left(\frac{1}{R^2} + \frac{1}{|Z|^2} \right)}{K^2} \quad (35)$$

where R is the resistor in the feedback of the operational amplifier used to convert the current into voltage, Z is the impedance of the MET cell, I_f^2 and U_f^2 are voltage and current noise spectrum density of the operational amplifier, respectively. To decrease the electronic self-noise, the transducer should have a high impedance and conversion factor. Also, low-noise operational amplifiers should be used. In all MET devices, the electronic self-noise contributes at relatively high frequencies.

Figure 12 shows the measured noise spectrum from a high-performance MET seismometer (CME-6211) in comparison with two high-performance, industry-grade broadband seismometers, the Streckheisen STS-2 and Trillium T240 units. The experiment is conducted at the Incorporated Research Institutions for Seismology (IRIS), Program for Array Seismic Studies of the Continental Lithosphere (PASSCAL) instrument center and EarthScope USArray array operations facility. The noise performance of the MET sensor is very similar with those high-performance devices up to periods of 60 seconds, demonstrating the feasibility of MET technology for broadband seismology.

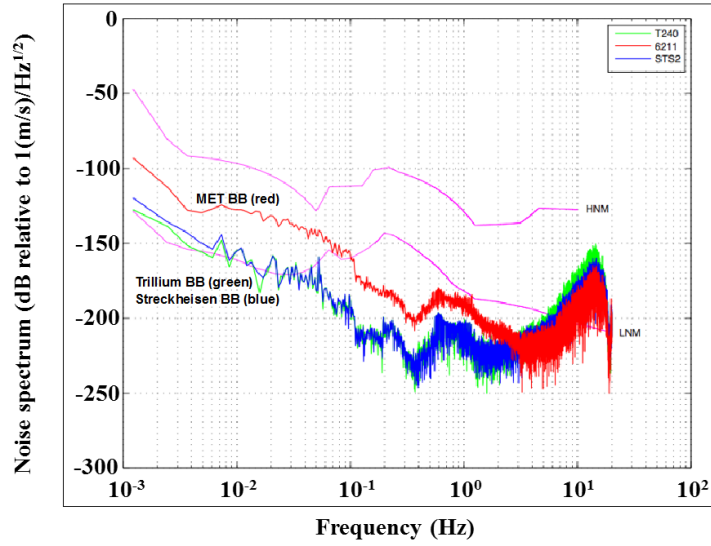


Figure 12. Noise performance of a MET seismometer (CME-6211) in comparison with high-performance, industry-grade broadband seismometers. Red: MET seismometer CME-6211; Blue: Streckheisen STS-2 broadband seismometer; Green: Trillium T240 broadband seismometer.

2.5. Different Types of MET Motion Sensor

Motion sensors based on MET technology include linear and angular accelerometers, rate sensors, gyroscopes and seismometers. Linear MET sensors can be configured for both horizontal and vertical sensing, as shown in Figure 13 (a and b).

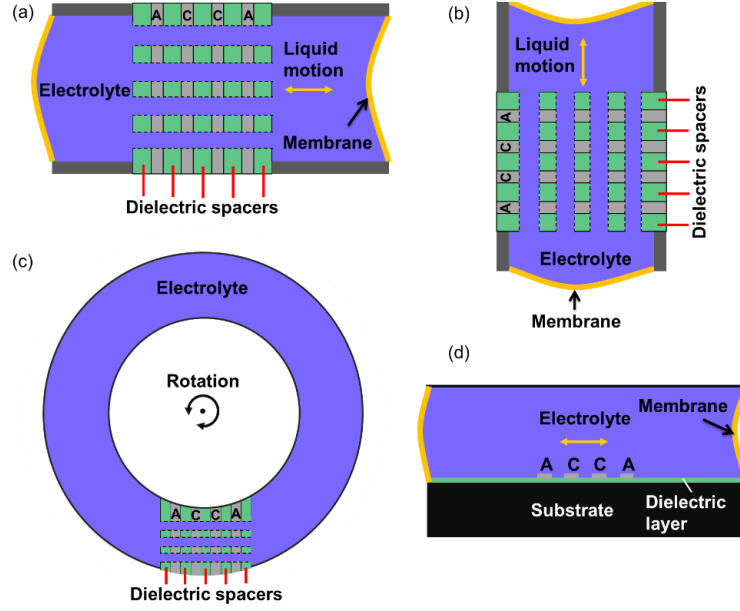


Figure 13. Schematic of different type of MET motion sensor.

In conventional MET sensors, platinum mesh and porous dielectric are adhesively bonded to form the electrodes and insulator layers illustrated in Figure 9. In addition to the sensing element, highly-flexible rubber membranes are manually assembled at the two ends of the channel to seal the electrolyte, providing restoring force for the mechanical subsystem. Examples of the performance parameters for commercially available MET linear seismic sensors are listed in Table 3. MTSS 1001 is a single-axis, ultra-compact, high gain, 1-Hz seismic sensor. MTSS 2003 contains three orthogonal oriented MTSS 1001 seismic sensors. It is probably the world smallest tri-axis 1-Hz seismometer. CME-6211 is a high performance MET seismometer, which is mentioned above. EP-300 is a very broadband seismometer by eentec [56].

Table 3. Current performance parameters for linear MET seismic sensors.

Performance	MTSS 1001	MTSS 2003	EP-300	CME-6211
Frequency range	1–300 Hz	1–300 Hz	0.0167–50 Hz	0.0167–50 Hz
Sensor Noise	50 ng/ $\sqrt{\text{Hz}}$	50 ng/ $\sqrt{\text{Hz}}$	10 ng/ $\sqrt{\text{Hz}}$	10 ng/ $\sqrt{\text{Hz}}$
Conversion Factor	300 V/(m/s)	300 V/(m/s)	2,000 V/(m/s)	2,000 V/(m/s)
Dynamic Range	>110 dB	>110 dB	150 dB at 1 Hz	135 dB
Non-linearity	<0.2%	<0.2%	Not specified	<1%
Orientation	Any direction	Any direction		Any direction
Weight	180 g	250 g	9.5 kg	7.5 kg
Temperature	“–40–+65 °C”	“–40 – +65 °C”	–12 – +55 °C”	–40 – +75 °C”
Power	<80 mW	<250 mW	<250 mW	<250 mW

Figure 14 shows an assembled 3-axis linear MET seismometer including two orthogonal horizontal sensors and one vertical sensor, along with the sensing circuits.

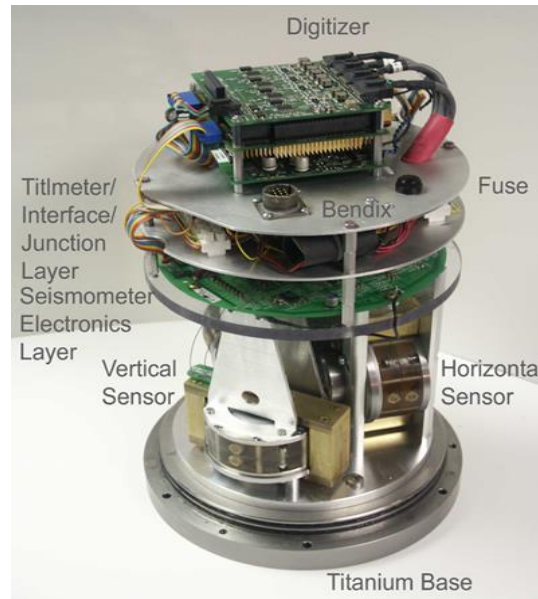


Figure 14. An assembled 3-axis linear MET seismometer including two orthogonal horizontal sensors and one vertical sensor, along with the sensing circuits.

Figure 13(c) shows the schematic of configuration of a rotary MET sensor. If an angular acceleration is applied as shown by rounded arrow, the electrolyte flows through

the sensitive element. This is another application of the technology. Currently the MET angular sensor is probably the only technology which commercially delivers highly sensitive rotational seismometers with a very low self-noise. Table 4 shows the key performances of current commercially available rotational seismometers (METR-03 and R2) [57-58].

Table 4. Current performance parameters for MET rotational seismometers.

Performance		METR-03	R2
Output		angular rate	angular rate
Noise at 1 Hz		$8 \times 10^{-7} \text{ rad/s}^2/\sqrt{\text{Hz}}$	$5 \times 10^{-7} \text{ rad/s}^2/\sqrt{\text{Hz}}$
Full Scale Range		0.1 rad/s	0.3 rad/s
Bandwidth		0.033-100 Hz	0.033 -50 Hz
Operating	Temperature	$-40 - +75 \text{ }^{\circ}\text{C}$	$-40 - +75 \text{ }^{\circ}\text{C}$
range			

The key advantages of MET sensors from other inertial sensors include, but are not limited to:

- (1) The inertial mass is a liquid (electrolyte solution flowing through the transducer) and no moving mechanics subject to wear out and possible damage, which makes the performance more reliable and enables inherent ability to withstand high shock forces.
- (2) The sensitivity of this sensor does not depend on the direction of sensitivity axis in space.
- (3) High sensitivity and low self-noise at low and ultra-low frequency ranges or even DC with the liquid inertial mass, properly selected parameters of the transducer and the proper structural design.

CHAPTER 3

MICRO SEISMOMETER BASED ON MOLECULAR ELECTRONIC TRANSDUCER TECHNOLOGY FOR PLANETARY EXPLORATION

Planetary seismology, the study of how seismic waves propagate within a planet, is particularly useful in determining its interior structure and composition. Much is known about the Earth's interior, thanks to advanced seismic instruments. Comparatively, little is known about the interiors of other terrestrial planets due to the difficulties in both instrument development and deployment. A planetary seismometer must first satisfy typical planetary instrumentation requirements, such as small size, low power consumption, and robust operation. Second, other terrestrial planets like Moon and Mars are expected to have much lower seismicity than Earth, meaning that the seismic signals of interest will be comparatively weak [59]. Therefore, low self-noise is a critical parameter for planetary seismometers. Furthermore, since planetary seismometers may experience a high deceleration as they land, they must be able to withstand very high shocks. Traditional wide-band spring-mass based seismometers are large, heavy, fragile, power-hungry, and most importantly require complicated installation due to the use of large solid suspended proof masses for thermal self-noise reduction [60]. Also, accurate installation is strictly required to ensure good ground coupling and alignment to the gravity direction. Capacitive solid-state spring-mass system based micro seismometers have been developed using MEMS processes to reduce the size of the traditional designs [30, 31]. They have limited successes because of the fragility and the inherent limitation of working mechanism of the solid-state mass-spring system, which still requires strict installation angle.

Although MET seismometers take the advantages that prove highly beneficial to planetary seismology, the conventional MET devices [50] developed and produced at present have a number of faults that ultimately limit their application range. The main ones are as follows:

- (1) High cost of transducer manufacturing;
- (2) High scatter of parameters of manually produced transducers resulting in the necessity of individual tuning of the corresponding electronics for each sensor, which also increases the cost of the device;
- (3) Early decrease in sensitivity of the sensor in the high-frequency range;
- (4) Very limited possibilities to optimize the cell parameters to decrease the instrument self-noise.

These shortcomings can be overcome by introducing MEMS microfabrication techniques to build the MET sensing element. The MEMS sensing element design to replace the current mesh core inside MET seismometer is shown in Figure 15 while the optimized geometrical parameters such as layer thicknesses, hole diameter and spacing, etc., which are closely related to performance parameters are determined on the base of modeling calculation results showing in Table 5. The sensing element consists of four metal (Platinum) electrode layers (gray) and five dielectric (Silicon Nitride) spacer layers, with an array of holes for electrolyte flow. Silicon substrate is patterned and etched away from backside using deep reactive ion etching (DRIE) to expose the holes to form the channels.

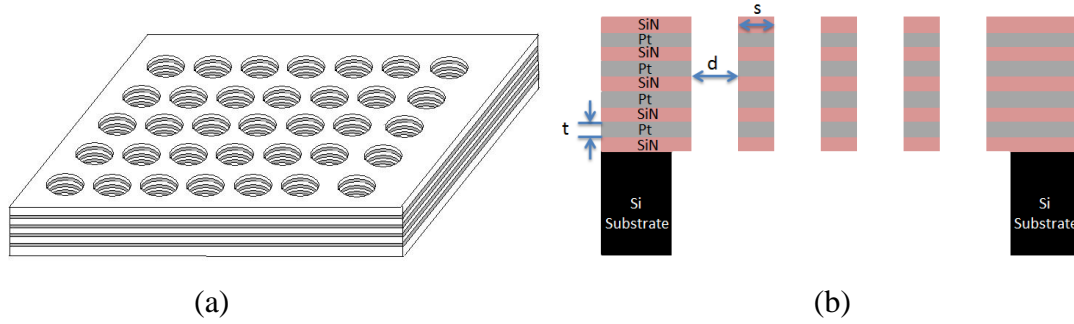


Figure 15. Schematic diagram of the sensing element, (a) Overview, (b) Cross-section view.

Table 5. Sensing cell parameters for the MEMS MET seismometer

Channel Diameter (μm)	Inter-electrode Spacing (μm)	Electrode Thickness (μm)	Number of Channels	Hydraulic Impedance ($\text{kg}/(\text{m}^4 \cdot \text{s})$)
50	1.0	0.2	1	3.9×10^{10}
40	1.0	0.2	20	4.8×10^9
40	1.0	0.2	50	1.9×10^9

3.1 MEMS Sensing Element Fabrication

3.1.1 Photoresist as Self-alignment Mask for Multi-layer Thin Film Deposition

Several micro-fabrication methods were tried to fabricate the seismometer sensing element. In the first one, photoresist AZ4620 was patterned to micro-pillars array on silicon substrate with thickness of 15 micrometers as a self-alignment deposition mask. Then the thin films (metal/insulator/metal/insulator) deposition was performed using Electron-beam evaporator. To validate the feasibility of this method, two double layers containing $0.5 \mu\text{m}$ Aluminum (Al) and $0.5 \mu\text{m}$ Silicon Dioxide (SiO_2) were deposited on the patterned substrate alternatively, followed by a lift-off process to remove photoresist using Acetone.

Therefore, after lift-off, previous photoresist-defined micro-pillars array finally became holes array. This process flow is shown in Figure 16. A scanning electron microscopy (SEM) image in Figure 16 was taken focusing on the sidewall of the holes fabricated by this method to examine the quality. The multi-layers could be observed in this SEM image, however, photoresist reflow happened during the thin films deposition and lift-off process resulting in deformation of the sidewall of holes. The step-like edge of sidewall observed from SEM image in Figure 16 was due to photoresist reflow and was not good for sensing.

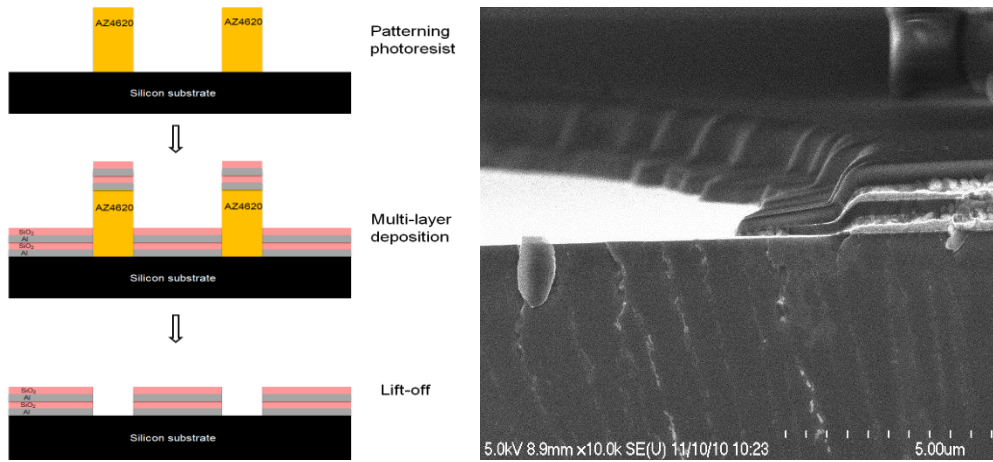


Figure 16. (Left) Diagrams illustrating the ideal fabrication process using AZ4620 photoresist as self-alignment mask for film deposition. (Right) Due to the deposition directionality problem, multi-layers at the edge are either not straight or covered too much by the next top layer.

Therefore, an alternative photoresist Microchem SU-8 2025 was used instead of AZ4620 to improve the sidewall profile and minimize the deformation. SU-8 is a much stronger photoresist than AZ4620 in terms of both physical and chemical properties. Also, it is a negative photoresist which provides better profile for lift-off process. The process is

similar as using AZ4620. First, Microchem Omni coat was span on to silicon substrate to allow easy stripping of hard to remove Su-8 photoresist during lift-off process and provide better adhesion between Su-8 and substrate. Then Su-8 was span with a thickness of 40 μm and both of Omni coat and Su-8 were patterned using photolithography. Multi-layer of Ti/Au (20nm/300nm) and 0.5 μm SiO_2 were deposited using E-beam evaporator and lift-off after patterning. However, images from holes formed by Su-8 lift-off process in Figure 17 show us that although the deformation phenomenon was improved and the profile of the sidewall is much sharper than the one fabricated using AZ4620, there was still a little deformation occurred on one side of the sidewall which can be explained by the combination of shadow effect of evaporator and Su-8 photoresist reshape.

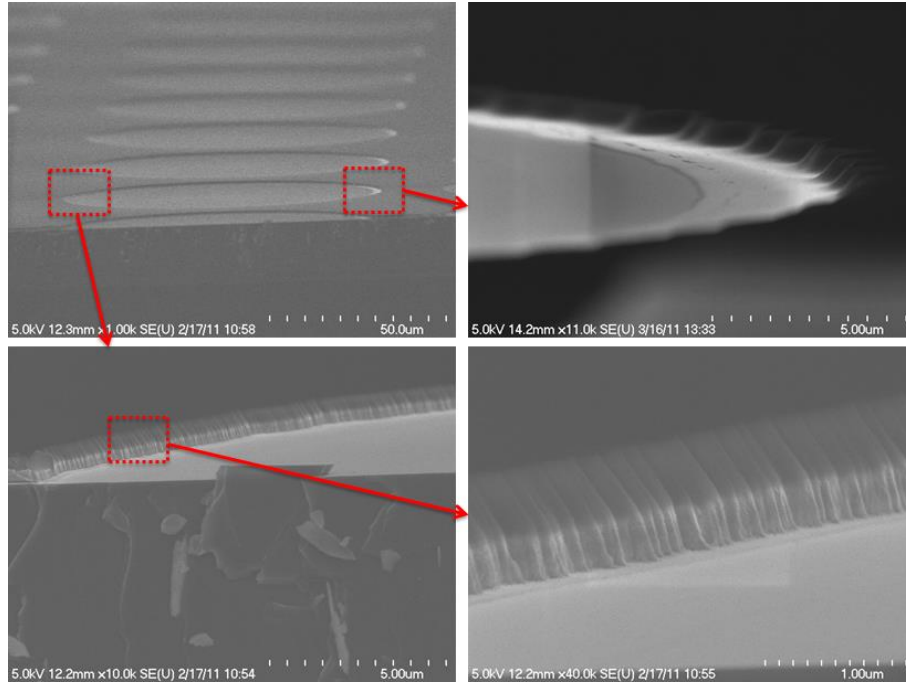


Figure 17. SEM images showing the holes array and sidewalls using the E-beam evaporation and lift-off process with Su-8 2025 photoresist as self-alignment mask for thin films evaporation.

3.1.2 Mechanical Micro-milling Machine

Since we had difficulties in fabricating holes array for sensing element using photoresist based methods, we moved to methods milling or etching from top of the multilayers. Micro-milling was one of those. Basically it is done by a precisely controlled physical milling machine which has capability of creating feature size down to micron meters in the surfaces of most materials. However, because the micro-milling machine we used was a physical milling machine, it damaged the surface a lot during the milling, and it cannot give us a sharp and smooth side wall for sensing purpose. Figure 18 shows SEM images of some holes micro-milled in a diameter of 100 μm and depth of 5 μm .

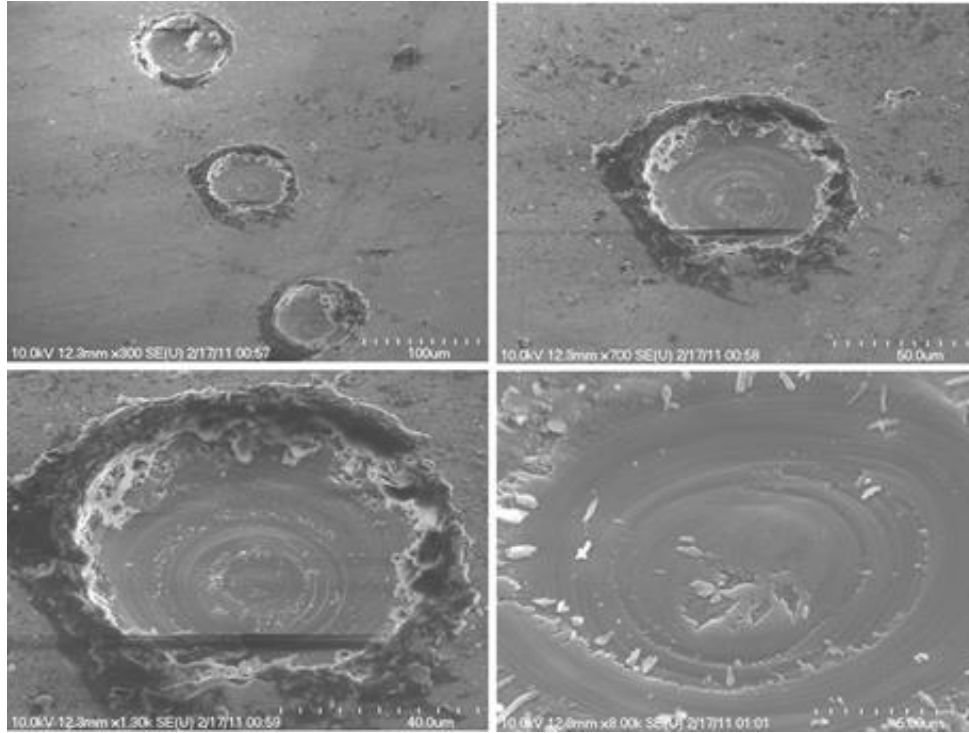


Figure 18. SEM images showing the holes fabricated by physical micro-milling machine. The sample surface and holes were damaged by milling.

3.1.3 Focused Ion Beam

Focused ion beam (FIB) systems operate in a similar fashion to a scanning electron microscope (SEM) except, rather than a beam of electrons and as the name implies, FIB systems use a finely focused beam of ions (usually gallium) that can be operated at low beam currents for imaging or high beam currents for site specific sputtering or milling. An FIB setup is a scientific instrument that resembles a scanning electron microscope.

Before milled by FIB system, the samples were prepared to have 9 layers with alternating silicon nitride (SiN) and platinum (Pt) layer

(SiN/Pt/SiN/Pt/SiN/Pt/SiN/Pt/SiN), with each layer 1 μm in thickness on top of silicon

substrate. After that, diaphragms with area of 1mm×1mm were patterned and etched all the way through the substrate from backside. Then, a FIB system, FEI NOVA 200, in the center of solid science at ASU was used to mill and image the holes array, which uses an energetic 30keV gallium ion beam with a 20nA beam current to mill the holes. The resulting structure could then be imaged by the electron beam assembled in it, shown in Figure 19. It shows a successfully milled 4 by 4 holes array with holes in diameter of 100 μm , and the detailed images of the sidewalls of the channels which have sharp profile and smooth surface. Although there is some re-deposition on the sidewall, it can be well cleaned by milling along the circle edge using lower current. Moreover, there is no short circuit between two platinum layers, which is very important for our sensing application.

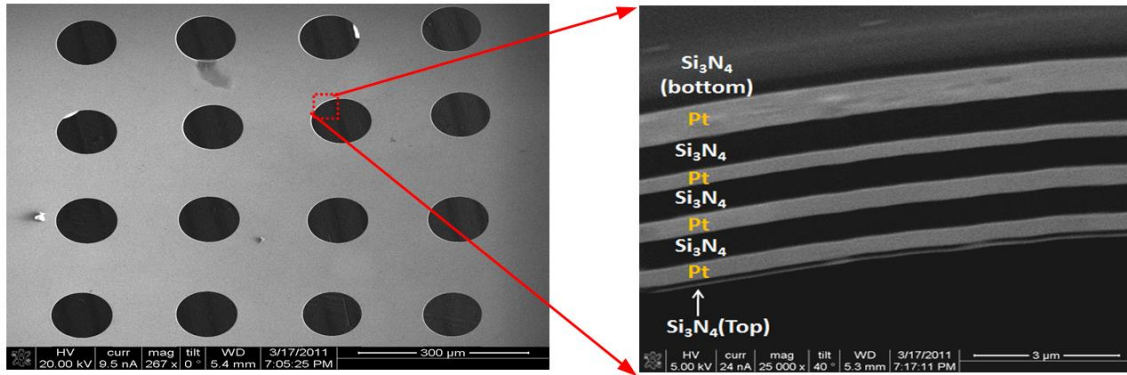


Figure 19. (left) SEM images of 16 holes fabricated with FIB on the diaphragm, (right) sharp and smooth side wall of hole showing 9 layers.

With the help of MEMS fabrication and FIB processes, we have been able to miniaturize the device and successfully achieve sharp and smooth channel sidewalls of the sensing element, and thus good alignment between the dielectric and electrode layers.

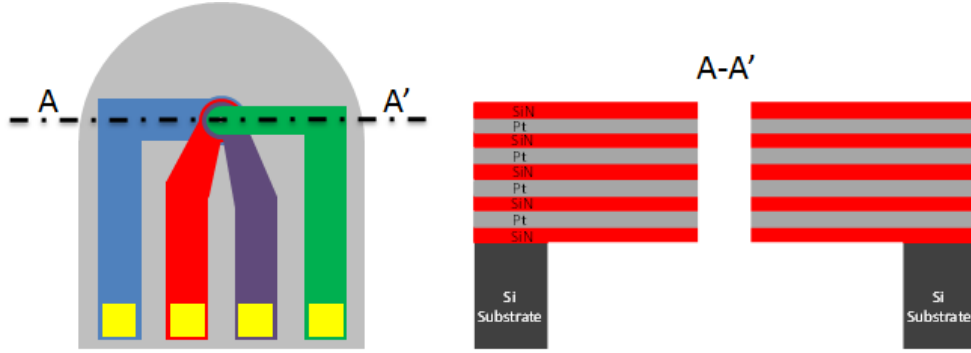


Figure 20. A schematic drawing of the finished micro seismometer sensing element (single channel).

A schematic drawing of finished sensing element is shown in Figure 20. Detailed fabrication processes of the micro MET seismometer core are shown in Figure 21. A double side polished silicon wafer ($500\ \mu\text{m}$ thick) with $0.6\ \mu\text{m}$ thick low pressure chemical vapor deposited (LPCVD) silicon nitride (SiN) layer on top forms the substrate and structural backbone of our device (Figure 21, (a)). Photolithography, metal evaporation and lift-off processes are used to pattern each layer of electrodes. First, AZ4330 photoresist is spun at 2000 rpm, followed by soft bake at 100°C for 90 seconds. EVG 620 aligner is used to expose the wafer with an energy dose of $300\ \text{mJ}/\text{cm}^2$. Then the wafer is developed in MIF 300 developer for 60-70 seconds. Oxygen plasma with power of 200 watts is used to ash the wafer for 1 minute to ensure that there is no photoresist leftover on the exposing area. Four electrodes are $10\ \text{nm}/200\ \text{nm}$ Ti/Pt layers deposited by E-beam evaporation and followed by lift-off using Acetone. Platinum is chosen as the electrodes because it is conductive yet chemically inert to the electrolyte containing *KI*. Four electrodes overlap only near the center of the device in order to minimize the risk that defects in dielectric layers would short two electrode layers. Each electrode is separated by a $1\ \mu\text{m}$ thick plasma enhanced chemical vapor deposited

(PECVD) low stress SiN dielectric layer processed at 350°C and branches to a separate contact pad used for electrical connection to the external circuitry (Figure 21, (b)). We choose SiN as the insulator material due to its low electrical conductivity, chemical inertness and low thermal mismatch to that of platinum. Reactive ion etching (RIE) is used to etch SiN to expose the electrodes' traces (Figure 21, (c)). An additional gold (Au) layer is selectively deposited on the traces from each contact pad to the central overlapping area to increase the electrical conductivity (Figure 21, (d)). Parylene-C with thickness of 20 μm is selectively deposited on top of gold traces to protect it from etching by electrolyte. Then, photolithography by backside alignment and deep reactive ion etching (DRIE) are used to etch the backside silicon. The DRIE stops as the reactive agents reach the bottom LPCVD SiN layer. The resulting thin diaphragm has a thickness of 5.8 μm . After that, a focused ion beam (FIB) system (Nova 200 NanoLab, FEI) is used to mill the through holes from front side to form the channels, exposing sidewall electrodes to the electrolyte filled in the channel (Figure 21, (f)). A high energy (20nA) rough milling and a low energy (3nA) fine cleaning are included in the FIB process. Finally, in order to clean the metal/dielectric redeposition on the surface of channel sidewall caused by the FIB milling process, a concentrated hydrofluoric (49% HF) acid etching of the milled device is performed in a vacuum environment for 90 seconds to trim the exposed dielectric layers on the channel sidewall 0.2 μm inwards to further avoid the shortage. Optical and SEM images of the fabricated devices are shown in Figure 22. Twenty devices are batch fabricated on one wafer. Figure 22(d) shows that the sidewall of the through hole milled by FIB and cleaned by HF has alternating graded Pt/SiN layers. Devices with multiple channels (through holes) are also fabricated by this method.

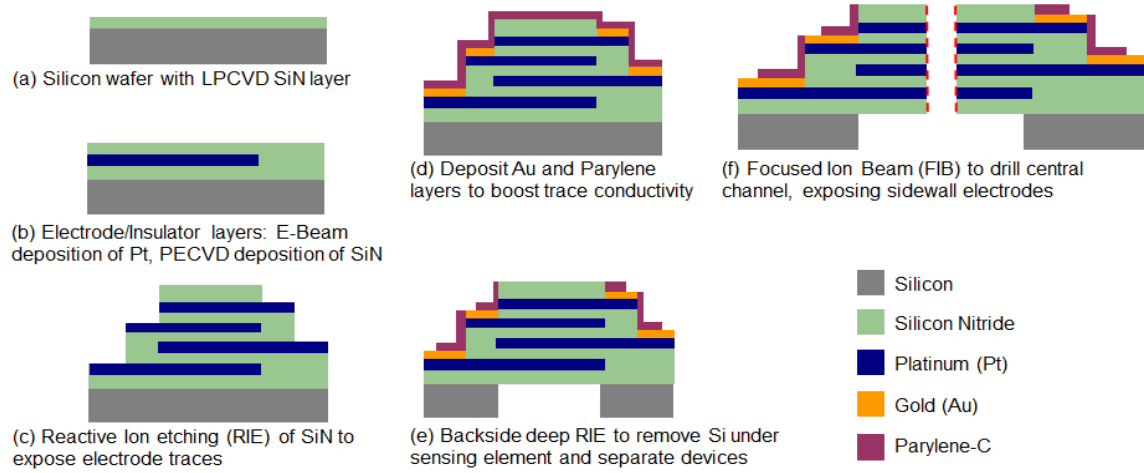


Figure 21. Detailed fabrication processes for the micro seismometer based on MEMS and METs technology.

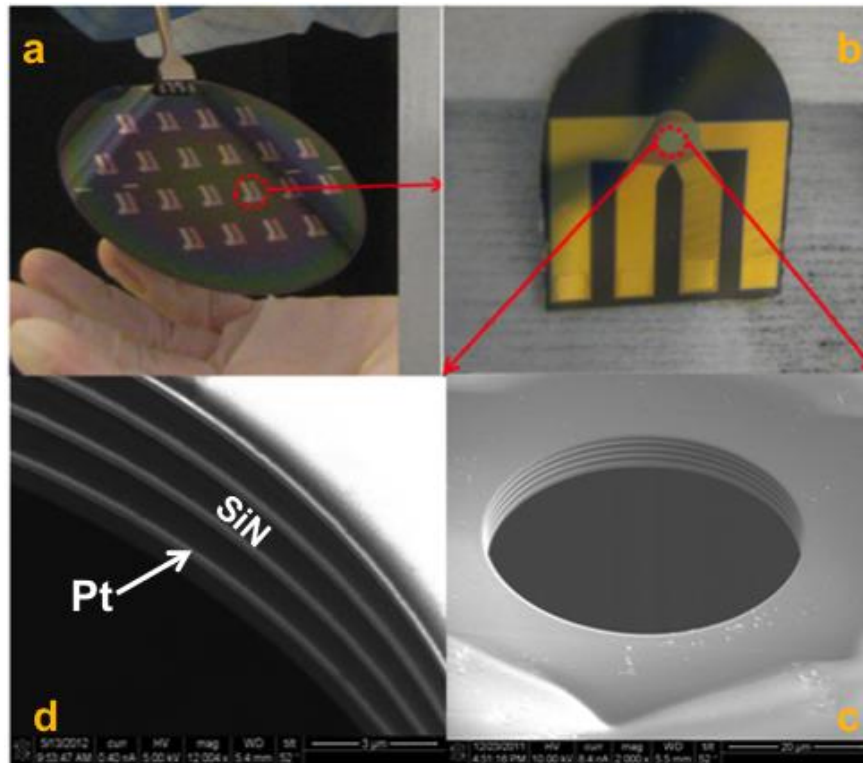


Figure 22. Photographs (optical and SEM) of a fabricated single-50 μm diameter-channel MEMS MET seismometer core. (a) 20 batch fabricated devices on one wafer. (b)

A single-50 μm diameter-channel micro MET seismometer core. (c) SEM image of the through hole milled by FIB on the 5.8 μm thin diaphragm. (d) SEM image of the side wall of the through hole, showing exposed alternating Pt and SiN layers.

3.2 Experimental Results and Discussion

3.2.1 Sensitivity

Three fabricated micro MET seismometer cores with different number of channels and channel diameter are assembled and mounted in seismometer housings, including electrolyte and control electronics. The chip with sensing cell is placed between two plastic housing, having a passing through channel. Ends of the channel were covered with flexible chemically inert rubber membranes. All assemble is pressed between two metal flanges. The junctions between chip and plastic parts are sealed with soft O-rings. The electrolyte is filled using vacuum method. The packaged device is assembled inside an air protecting shell. The whole assembly is shown in Figure 23. The cell output signal is measured by an amplification circuit consisting of two trans-impedance amplifiers which convert current signals from two cathodes to voltage with a conversion coefficient of 100 $\text{k}\Omega$ and followed by a differential amplifier which transforms the difference between the two converted signals into output voltage.

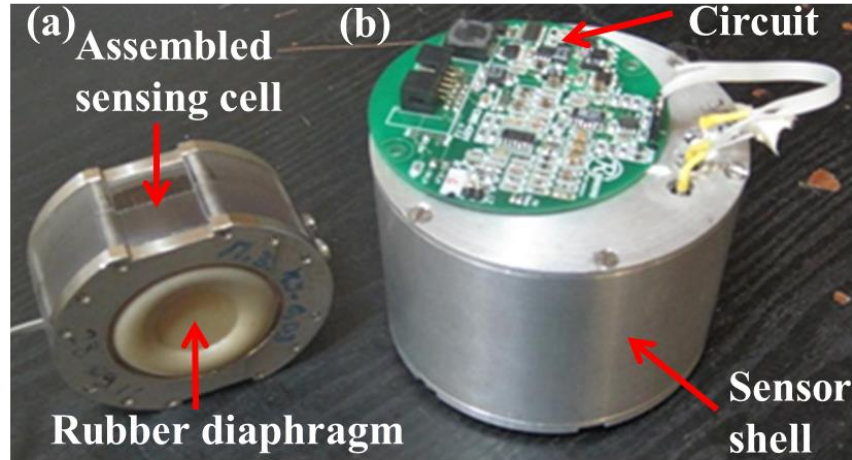


Figure 23. Assembled sensing cell for a MEMS MET seismometer.

Table 6 lists the configurations of the fabricated devices and their corresponding R_h scale factor. The scale factor of R_h is defined 100% for the single-50 μm diameter-channel device (Device 1).

Table 6. Configurations of three fabricated MEMS MET seismometers.

	Number channels	of Channel diameter	Scale factor of R_h
Device 1	1	50 μm	100%
Device 2	20	40 μm	12.5%
Device 3	50	40 μm	5%

The testing assembly is then placed on the motion exciter and frequency response is determined by the harmonic scan method. The devices under test are sequentially subjected to a series of excitations whose amplitude is constant in acceleration units and the frequency covers the range of interest (0.08 - 80 Hz). In units of Earth's surface gravity G , the excitation amplitude is 400 μG in the long period range (0.08–8 Hz) and 1000 μG in the short period range (12–80 Hz). Figure 24 shows that under an optimum

bias voltage of 600 mV, the sensitivity of device 1 reaches a peak value of 809 V/(m/s²) at 0.32 Hz, and greater than 100V/(m/s²) over frequency range of 0.08-16 Hz. Figure 25 shows the sensitivity frequency response for the devices with different configurations listed in Table I. It is seen that as R_h decreases from device 1 to 3, the sensitivity magnitude increases at all frequencies. The maximum sensitivity is 809 V/(m/s²) for device 1, while this number increases to 3690V/(m/s²) for device 3 whose R_h is 5% of that of device 1. This is reflected by the transfer function of the mechanical subsystem of the device (Equation (24)). Another reason is that the increased surface area of the electrodes exposed to the electrolyte from device 1 to 3 results in an increase in the output signal, and thus the sensitivity.

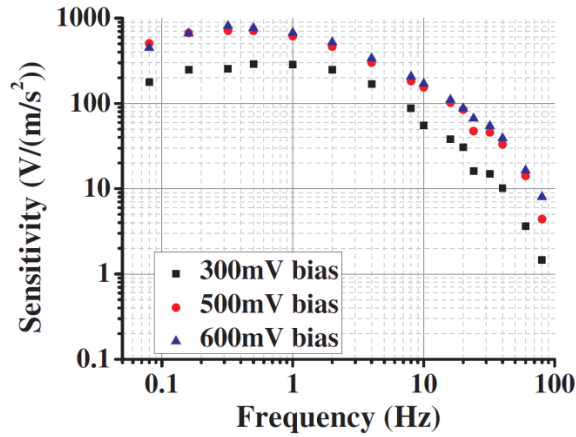


Figure 24. Measurement results of sensitivity frequency response of a fabricated micro MET seismometer (device 1) in different bias conditions.

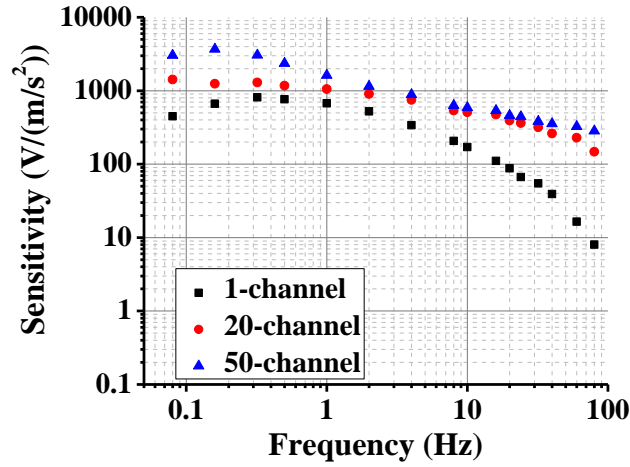


Figure 25. Comparison of the sensitivity frequency response for three MEMS MET seismometers in different configurations. Black, device 1; Red, device 2; Blue, device 3.

3.2.2 Linearity

The linearity tests are performed by changing the input signals. In order to estimate the maximum linearity range of the sample, the input signals are set larger than those in above sensitivity tests. The observed scale factor behavior is shown in Table 7. Here the scale factor calculated at smallest applied signal is defined as 100% level. As the input signal increases, the scale factor decreases very slowly for relatively small inputs. Finally, a very non-linear behavior is observed at input signals higher than 2mg at 8 Hz, where a dramatic drop of scale factor can be seen. Based on Table I, the linear range for the sensor is limited to 2mg level. Practically, the linear range can be expanded by 1–2 orders of magnitude without any changes in the sensing cell design if a negative feedback mechanism is implemented.

Table 7. Scale factor vs. acceleration.

Input signal at 8 Hz	1.5 mm/s ²	6 mm/s ²	12 mm/s ²	30 mm/s ²	60 mm/s ²	120 mm/s ²
Scale factor	100%	98.8%	98.1%	5.8%	6.8%	5.8%

3.2.3 Noise

Noise test of the micro MET seismometer is conducted in the underground vault.

The tested noise power spectrum density (PSD) curves for all three devices listed in Table 6 are shown in Figure 26, in comparison with a commercialized CMG-40T seismometer (Guralp Systems Ltd.).

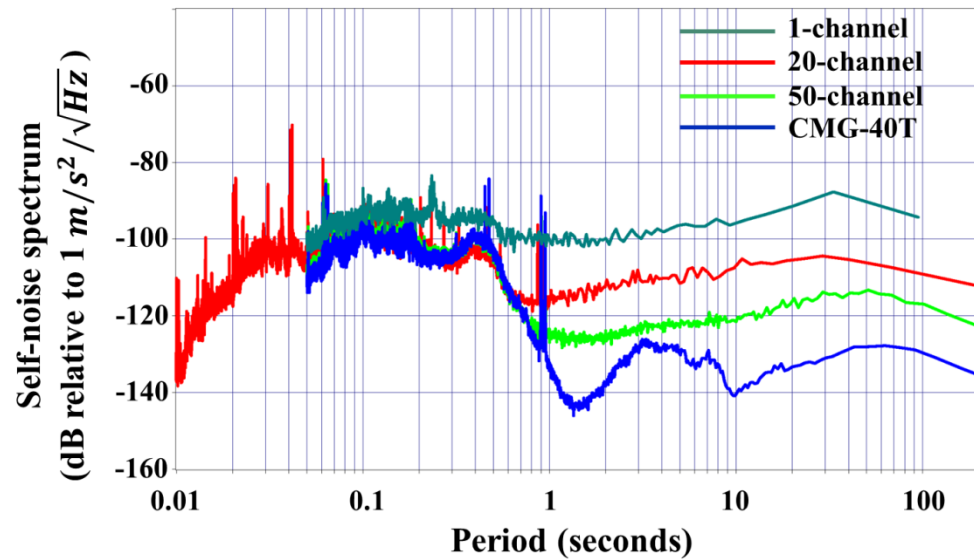


Figure 26. Noise PSD filtered in 0.01 – 50 Hz frequency range of fabricated single-50 μ m diameter-channel, 20-40 μ m diameter-channel and 50-40 μ m diameter-channel micro MET seismometers, in comparison with CMG-40T seismometer.

The conclusions can be drawn from the data presented:

i) Decreasing of R_h results in significant decrease in noise. The noise PSD achieves -100 dB ($1.0 \mu g/\sqrt{Hz}$) at 1 Hz for device 1. Device 2 whose R_h is 1/8 that of device 1 shows a 15dB decrease in noise, with -115dB ($0.18 \mu g/\sqrt{Hz}$) at 1 Hz. Device 3 whose R_h is approximately 1/20 that of device 1 shows 27dB decrease in noise, with -127dB($44.6 ng/\sqrt{Hz}$).

ii) The noise spectrum is not flat in the frequency range and demonstrates a behavior close to $1/f$ type at low-frequency end. The noise level is higher than predicted by Equation (31) at all frequencies. Such behavior shows that the primary contributor to the noise for the tested devices is $1/f$ noise of the electronic components.

CHAPTER 4

ALTERNATIVE FABRICATION METHODS OF MICRO SEISMOMETER BASED ON MOLECULAR ELECTRONIC TRANSDUCER USING SILICON ON INSULATOR PROCESS TECHNOLOGY

From the experiment results showing in Chapter 3, it has been concluded that the noise performance of the micro MET seismometer is heavily depends on the hydrodynamic resistance of the device. According to Eq. (32) in Chapter 2, the hydrodynamic resistance of a channel is inversely proportional to the 4th order of the radius of the channel cross-section and the number of parallel channels, and proportional to the length of the channel. Therefore, I have been attempting to increase the number of channels and the radius of the channel cross-section on the original design of the micro MET based seismometer described in Chapter 3, trying to improve the noise performance. However, these attempts have limited successes because of the limitation of FIB process and the thin diaphragm. First, FIB milling process is very time consuming and costly. For instance, a 50-channel device takes more than 20 hours to finish FIB process including initial milling and fine cleaning. Second, the quality of the FIB milling is dependent on how clean one can remove the re-deposited material during the milling to avoid short circuit between each electrodes. For a one or two-channel device, it is easy to ensure the quality by finely cleaning each channel. However, as the number of channels increases, the yield of the device becomes lower. Third, as the diaphragm where the FIB milling is performed is very thin (~6 μm), it is easy to break when the radius of milling goes beyond 100 μm , or when the number of milling channels goes above 50. It is also

not practical to increase the diameter of the thin diaphragm infinitely. Moreover, FIB can only process one device at a time. So, essentially, the whole fabrication process involving FIB is not a batch fabrication process. In order to overcome the above limitations to further improve the noise performance, as well as to make the devices batch fabricated, I developed two alternative fabrication processes based on SOI (silicon on insulator) wafers, which will be described below.

4.1 Single-SOI Fabrication Process

A new fabrication process of the sensing element of micro MET seismometer is developed to overcome the above limitations as shown in Figure 27. It starts with a SOI wafer with a thick device layer (150 μm) and box layer (5 μm) as a substrate. First, photoresist AZ4620 is patterned on the backside of the SOI wafer and used as mask for deep reactive ion etching (DRIE) of silicon handle layer to form part of the channel. In order to ensure the symmetry of the electrodes, DRIE is performed under precise control which stops when the remaining thickness of the handle layer is equal to that of the device layer. Second, the top silicon device layer is patterned to be circles with 200 μm diameters using AZ4620 which is also used as mask for DRIE of the top silicon. This time, DRIE is performed until it reaches the box layer (SiO_2) of the SOI wafer. Then the remained photoresist along with the silicon will act as mask for wet etching SiO_2 . The undercut of the SiO_2 is desired for the subsequent isolation between electrodes. Then, the remaining silicon will continue to be etched by DRIE to open through the entire channels. Next, photoresist is removed and electrode (Ti/Pt) will be E-beam deposited onto the top and bottom surface of silicon, and sidewall of the channel as well. By tuning the angle

between the metal source and the target wafer, the sidewall of SiO₂ recess is ensured to have no metal deposition. Finally, two of the above fabricated wafers are selectively coated with Parylene-C layer and adhesively aligned and bonded to form the sensing element with four isolated electrodes.

This process allows significant increase in the strength of supporting structure, the diameter of the channels (200 μm) and the number of channels (800). Meanwhile, it does not have FIB process involved, and the devices can be fabricated in batch, thus greatly reduces the fabrication cost and time. However, the trade-off would be the rougher sidewall surfaces and imperfect alignment.

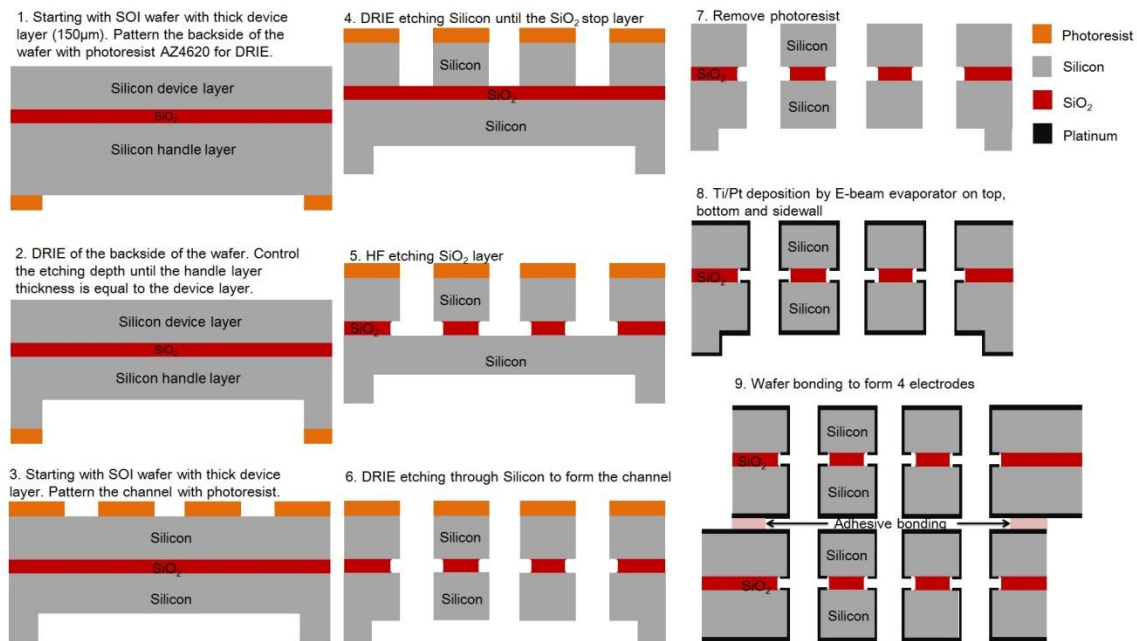


Figure 27. Fabrication processes of the sensing element of MET based micro seismometer with single- SOI wafers.

4.2 Double-SOI Fabrication Process

Although the above single-SOI process overcomes some of the limitations of FIB involved process, increases the diameter and numbers of the channels, the channel length is still long, which may degrade the noise performance. Single-SOI wafer with thinner device layer could be used to reduce the length, however, since the backside of the SOI wafer does not have etching stop, the depth of the backside DRIE is hardly to control, especially when the remaining silicon layer is less than 10 μm . To further reduce the channel length so that further decrease the hydrodynamic resistance, another alternative approach is come out.

In this case, double-SOI wafer is used as starting point with device layers of $DT=DM=5\text{ }\mu\text{m}$, and box oxide layers of $BT=BM=2\text{ }\mu\text{m}$. The double-SOI wafer has two Si device layers with precise thickness and bottom box layer as etching stop, which provide better symmetry of the configuration of anodes and cathodes. The fabrication processes are demonstrated in Figure 28. A 0.6 μm thick LPCVD SiN layer is deposited on both sides of the double-SOI wafer. First, backside of the wafer is patterned by photolithography and followed by reactive ion etching of the exposing SiN. Second, the above patterned SiN layer is acting as hard mask for TMAH etching of Si until it stops at the bottom box layer. RIE of the bottom box layer is followed to expose the middle device layer and photoresist is spun on to the etched structure as protection from the following etching processes. Third, channels are patterned from topside by photolithography and followed by RIE etching of SiN etching. DRIE instead of TMAH etching of Si is used this time to form vertical channels. After the DRIE reaches the top box layer, HF isotropic etching of box layer is performed to form the undercut which is

desired to isolate two electrodes. Then, DRIE will continue to etch the exposed bottom device layer until the whole channel opening is etched through. Similar to the single-SOI processes, rotated E-beam evaporation of thin metal of Ti/Pt is conducted to form electrodes on top, bottom, sidewall of the channel, except the undercut area. Finally, Parylene-C adhesive layer is selectively deposited and two above fabricated wafers are adhesively bonded with alignment to complete the device.

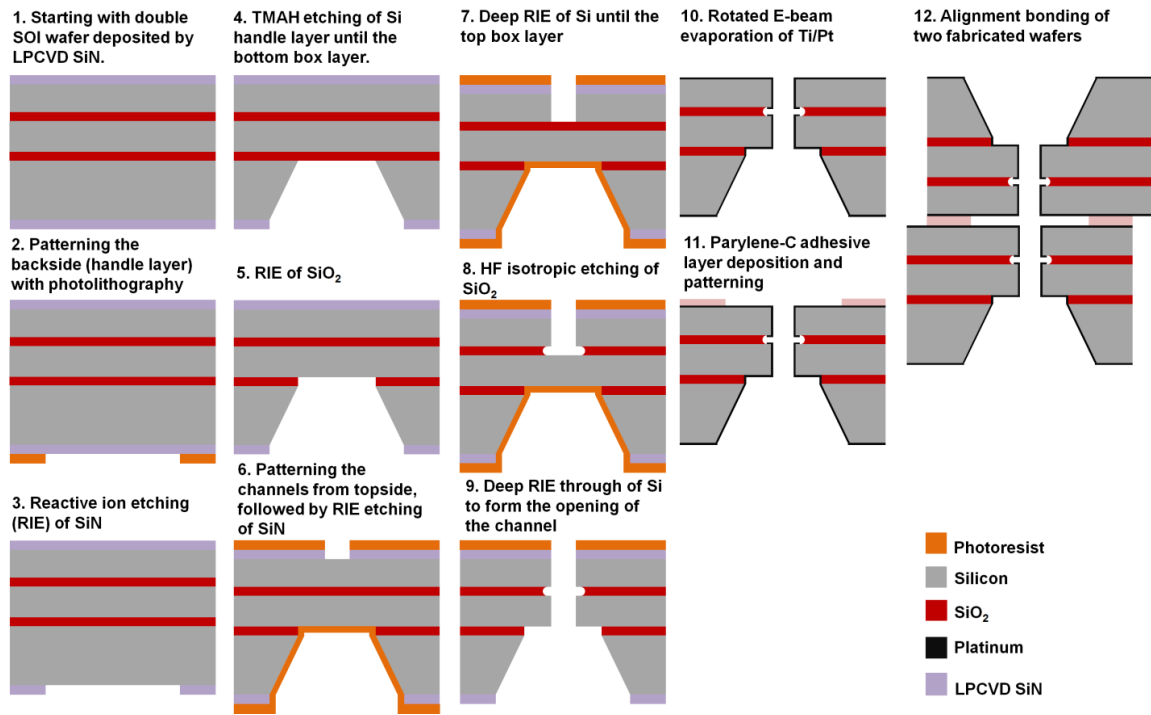
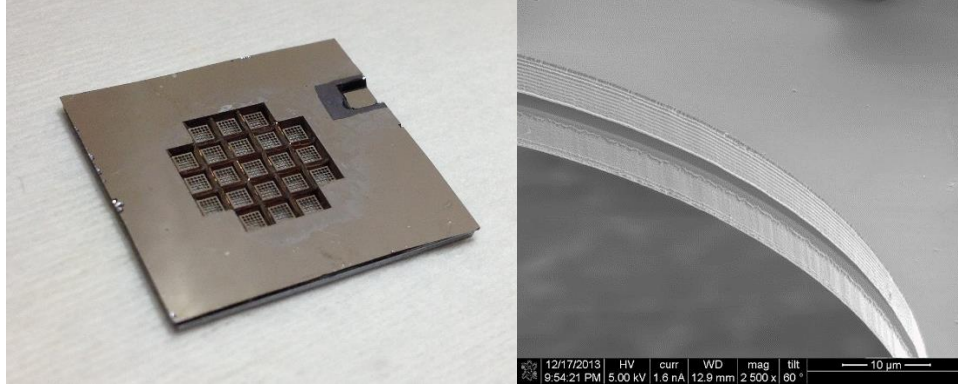


Figure 28. Fabrication processes of the sensing element of MET based micro seismometer with Double-SOI wafers.



(a)

(b)

Figure 29. Photograph of a fabricated device with double-SOI process (a), and a SEM image showing the metal (Ti/Pt) coverage on the sidewall of the channel including silicon and the recessed SiO₂.

Figure 29 shows a fabricated device using double-SOI process. The size of the device is 17.5mm by 14.5mm and 1.1mm thick. In one of the bonding pairs, the bottom KOH patterns are 2mm squares. The holes from topside have diameter of 200 μm and spacing of 50 μm. The number of holes in one square diaphragm is 25 and there are 21 diaphragms. So the total number of holes for the device is 525. In this case, the hydrodynamic resistance $R_h = 1.16 \times 10^6 (\text{N} \cdot \text{s})/\text{m}^5$, which is 30000 times lower than a single-50 μm-diameter channel device developed in previous design [61] described in Chapter 3. So the self-noise is expected to be much lower. Figure 29 (b) shows a zoom-in SEM image of the metal coverage of the recess of the SiO₂ fabricated from step 8 through 10. There is a clear boundary between the deposited and un-deposited area, which proves that due to shadow effect, the sidewall of silicon is covered well by metal, but the

sidewall of the recessed SiO_2 is not covered by metal. Therefore, the two electrodes are insulated.

CHAPTER 5

MET-BASED LOW FREQUENCY ACCELEROMETER WITH POST-CMOS COMPATIBLE PROCESS USING DROPLET AS SENSING BODY

Accelerometers with small size, low noise and high sensitivity at low frequencies are important in a broad range of disciplines including seismology and resource detection in the oil industry. As mentioned in chapter one, most micro solid-state accelerometers are developed with fundamental mechanism as a mass-spring system consisting of a suspended proof mass. Their low frequency performance is relatively low due to the intrinsic limitation of working principles of mass-spring system. Inspired by the exceptional ability to convert mechanical signals to electric current in electrochemical systems, pioneering studies of liquid-state motion sensors based on MET provide an alternative paradigm. As opposed to solid-state accelerometers, MET accelerometers use a liquid-state inertial mass. The MET transducing electrochemical cell (Figure 30) consists of the sensing channels with four electrodes separated by dielectric spacers and a highly-flexible rubber diaphragm. A concentrated iodine-iodide electrolyte is filled in the channel acting as the inertial proof mass. Compared to solid-state accelerometers, MET accelerometers have no moving solid mechanical parts subject to possible damage, enabling inherent ability to withstand high shock. In addition, they have high sensitivity and low self-noise in the low frequency range with properly selected parameters of the transducer.

However, despite the rather high output parameters obtained, the conventional MET devices have a number of limitations including high cost, high scatter of parameters

due to manual production of transducers requiring individual tuning of corresponding electronics for each sensor, early decrease in sensitivity in the high frequency range due to large internal dimensions, and restricted possibilities to optimize the performance. These shortcomings motivated the development of a MET sensor employing MEMS techniques which reduces the device size and improves the sensitivity and reproducibility and gives the possibility of optimization by tuning the physical parameters during fabrication [61]. However, the three-dimensional structure of the device in [61] provides great challenges in fabrication and packaging, which is also costly due to the involvement of focused ion beam milling. More importantly, the fabrication process is not CMOS-compatible and hard to integrate into modern electronic system. Therefore in this chapter, a droplet-based horizontal MEMS MET accelerometer made with a post-CMOS compatible microfabrication process with high-volume manufacturing compatibility is developed [63]. This device combines the advantages of both MET and MEMS technology. In addition, its post-CMOS-compatible fabrication processes which only contain deposition of four electrodes on a planar substrate, is much simpler compared to solid-state CMOS MEMS accelerometers [17, 18, 19, 20, 21, 22, 23] which include complicated fabrication of mass-spring system. Furthermore, the novel idea of using an oil film as the sealing diaphragm eliminates the complicated three-dimensional packaging.

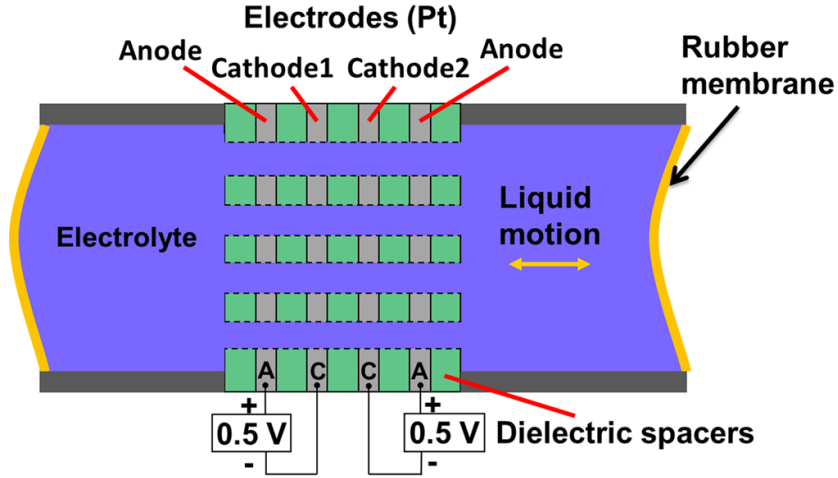


Figure 30. Schematic of a traditional MET accelerometer using standard-machined platinum mesh separated by dielectric grids as sensing cell. The sensor is manually assembled with highly-flexible rubber diaphragms.

5.1 Device Fabrication

The schematic of the device is illustrated in Figure 31, consisting of a planar four-electrode (Anode-Cathode1-Cathode2-Anode) MET cell located in a solid rectangular housing channel on a silicon substrate with low pressure chemical vapor deposited (LPCVD) silicon nitride (SiN). It is shown that this structure has promising performance comparable with ring electrodes in open holes when the device size is reduced to micro-scale [50].

Figure 32 details the fabrication processes. First, four electrodes made of 10nm/100nm Ti/Pt are deposited by E-beam evaporation and patterned with standard planar photolithography and a lift-off process, with electrode width of $h = 100 \mu\text{m}$ and inter-electrode spacing of $d = 30 \mu\text{m}$ [Figure 32(b)]. Second, surface modification is performed to reduce the hysteresis of droplet deformation. Lift-off process is applied to

coat the electrodes with the hydrophobic CYTOPTM thin film and patterned such that there is a hydrophilic spot surrounded by hydrophobic areas [Figure 32(c)]. A rectangular glass housing is adhesively bonded to the device surface to form the channel with 1 mm in both width and height [Figure 32(d)]. Prior to the final assembly of the device, a 0.8 μL concentrated iodine-iodide electrolyte droplet and a small amount of mineral oil are sequentially dispensed by micropipettes in the hydrophilic area covering platinum electrodes [Figure 32(e)]. This oil-encapsulated electrolyte droplet replaces the complex three-dimensional assembly of soft membranes and electrolyte in [61] and acts as the sensing body. The oil not only prevents the droplet from evaporating, but also works as the elastic diaphragm to contain the droplet, which allows it to be stabilized in the center. Finally, the top glass ceiling is assembled [Figure 32(f)]. The fabrication process as well as the packaging is simple and compatible with batch processing.

5.2 Operation Principle

Similarly with traditional and MEMS MET seismometers discussed in previous chapters, when an electric potential (0.5V) is applied to the anode-cathode pairs, an electrochemically-induced current based on reversible electrochemical reactions between anodes and cathodes appears regardless of the presence of mechanical motion of the droplet [50]. In the presence of an external acceleration, the droplet moves relative to the electrodes due to inertia. Besides diffusion, an additional convective transport of ions between the electrodes occurs, resulting in a significant change in the concentration gradient near the electrode surface, and hence a change in the output current. The

amplitude of the differential cathode current provides the signal read-out [50]. The equation that governs motion of the electrolyte droplet is,

$$\frac{d^2V}{dt^2} + \frac{R_h S_{ch}}{\rho L} \frac{dV}{dt} + \frac{k}{\rho L} V = -S_{ch} a \quad (36)$$

where V is the volume of fluid passing through the channel, a is the external acceleration, R_h is the hydrodynamic resistance which is solely determined by the fluid viscosity and the channel geometry in laminar flow condition [61], k is the coefficient of volume stiffness and depends only on the characteristics of the oil film, ρ is the density of the droplet, S_{ch} is the cross-section area of the channel and L represents the length of the droplet. The $(R_h S_h/\rho L) dV/dt$ term in Equation (36) shows that the damping is proportional to the flow rate associated with the hydrodynamic resistance R_h . The $kV/\rho L$ term describes the restoring force from the oil.

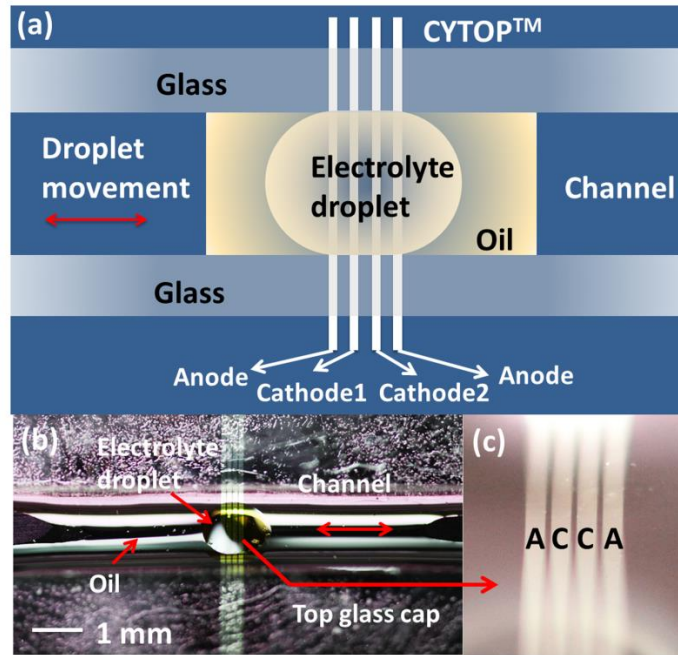


Figure 31. Overview of the electrolyte droplet-based MET accelerometer: (a) Top view schematic of the device. (b) Sensing element of the fabricated device, (c) Zoom-in view of the droplet-covered electrodes.

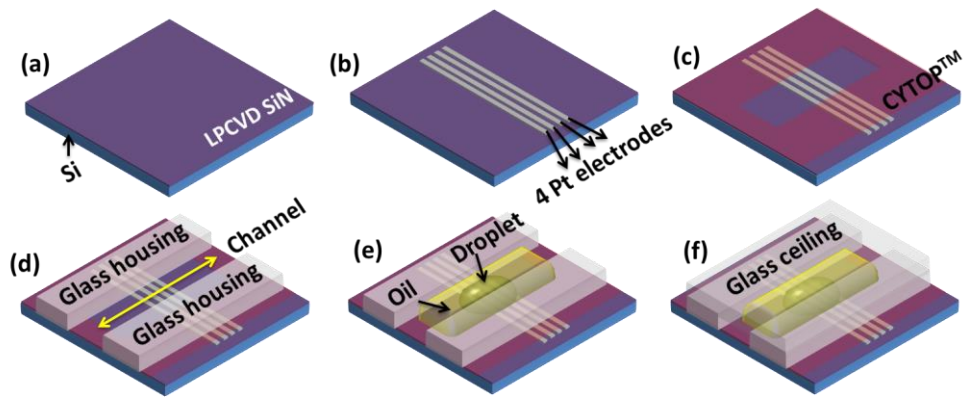


Figure 32. Microfabrication processes of the post-CMOS-compatible MEMS MET accelerometer.

By transforming Equation (36) to the frequency domain and using an approximated expression of the electrochemical transfer function of MET in the frequency domain [62], the overall frequency-dependent transfer function of the device which is a superposition of the transfer functions of the mechanical and electrochemical systems can be obtained as

$$|H(\omega)| = \frac{\rho L}{\sqrt{\left(\frac{\rho L}{S_{ch}}\right)^2 \frac{(\omega^2 - \omega_0^2)^2}{\omega^2} + R_h^2}} \cdot \frac{C}{\sqrt{1 + \left(\frac{\omega}{\omega_D}\right)^2}} \quad (37)$$

where $\omega_0 = \sqrt{k/\rho L}$ is the mechanical resonant frequency of the device, C (A/(m³/s)) is the conversion factor of the electrochemical cell, $\omega_D = D/d^2$ is the diffusion frequency with inter-electrode distance d , and diffusion coefficient D . It can be seen from Equation (37) that there are two poles in the transfer function: ω_0 and ω_D , determining the low/high cutoff frequency and bandwidth. One of the advantages of scaling down in d is that the resulting significant increase in ω_D enables $\omega_D \gg \omega_0$ and therefore the high cutoff frequency above which the sensitivity starts to decay significantly is increased and the bandwidth is broadened.

5.3 Experimental Results

Experimental validation is conducted using a device with $d = 30 \mu\text{m}$, $h = 100 \mu\text{m}$ and $R_h \approx 5 \times 10^7 \text{ kg}/(\text{m}^4 \cdot \text{s})$. The sensor is mounted on a vibration exciter which can generate sinusoidal vibration with controlled frequency and acceleration. The acceleration is monitored *in situ* using a reference accelerometer (ADXL203, Analog Devices [25]). The output voltage of the device under controlled acceleration at 20 Hz

[Figure 33] shows that within 0.6 G acceleration range, the measurement sensitivity has a constant value of 10.8 V/G. The sensor is then sequentially subjected to a series of excitations whose amplitudes are approximately constant (0.35 G) covering 1 – 200 Hz frequency range. The measured normalized frequency response of the device with a nearly flat response in the low frequency range of 1-50 Hz is shown in Figure 31. The normalized experimental result fits well with the analytical one by setting $R_h = 4 \times 10^7 \text{ kg}/(\text{m}^4 \cdot \text{s})$, $d = 30 \text{ } \mu\text{m}$, $D = 2 \times 10^{-9} \text{ m}^2/\text{s}$ (for iodine-iodide electrolyte) and $f_0 = 40 \text{ Hz}$ in Equation (37). It is indicated from Figure 34 that Equation (37) is sufficient to model the dynamic behavior of the device. Figure 35 presents the measured spectrum of the accelerometer output under a 20 Hz, 0.35 G sinusoidal acceleration ($n=5$). The equivalent input-referred noise floor is $75 \text{ } \mu\text{G}/\sqrt{\text{Hz}}$, given that the sensitivity at 20 Hz is 10.8 V/G. The noise level of a MET sensor is proportionally determined by R_h . Potential methods to reduce R_h (improve noise performance) include increasing the cross-section area of the channel, or introducing a hydrophobic surface modification to the channel wall. The main fabrication variations that affect the device performance come from the use of micropipette to dispense the electrolyte droplet and oil. The resulting variations of the droplet mass and the spring constant (k) will affect the resonant frequency and cause the shift of sensitivity curve. As shown in Figure 34, the resonant frequency is shifted to $\sim 30 \text{ Hz}$ and $\sim 25 \text{ Hz}$ when $\sim 150\%$ and $\sim 200\%$ electrolyte droplet volume are applied, respectively. Therefore, it is critical to precisely control the volume of the droplet and oil for optimized repeatability of the sensors.

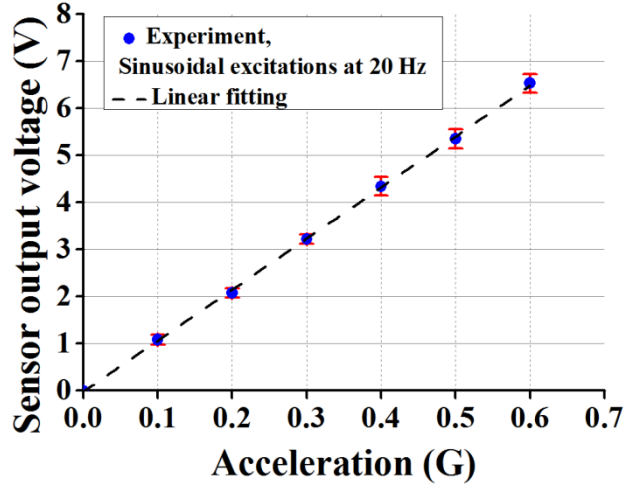


Figure 33. Experimental result of sensitivity of the device under 20 Hz sinusoidal input accelerations within 0.6G magnitude.

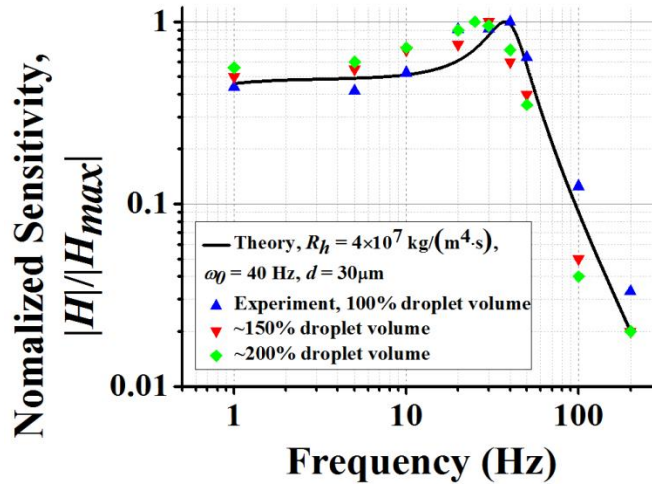


Figure 34. Experimental result of the normalized sensitivity frequency response of the device in comparison with the theoretical analysis. Resonant frequency is down shifted to ~30Hz and ~25Hz when ~150% and ~200% electrolyte droplet volume are applied, respectively.

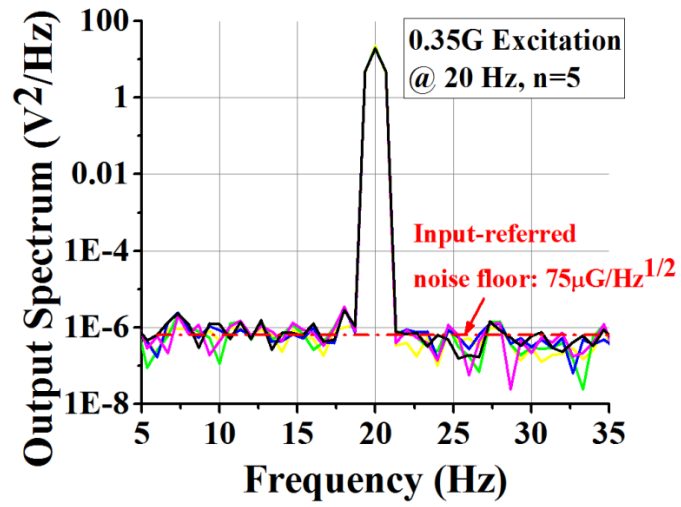


Figure 35. Measured output signal spectrum under a 0.35 G sinusoidal excitation at 20 Hz (n=5), showing an input-referred noise floor of $75 \mu\text{G}/\sqrt{\text{Hz}}$.

CHAPTER 6

SUMMARY AND FUTURE WORK

This thesis mainly focuses on design, fabrication and testing results of the micro MET based seismometer and accelerometer. In Chapter 1, the background and history of development of the seismometers are introduced. The basic working principle of the mass-spring system which is the core of the solid-state seismometer/accelerometer is discussed. Inspired by the MEMS capacitive accelerometer, which is also introduced, people have been trying to miniaturize the traditional seismometer to expand its applications to planetary exploration. However, those efforts have limited successes due to the inherent limitation of the solid-state mass-spring system. Therefore, in Chapter 2, a new motion sensing mechanism called molecular electronic transducer is introduced including its operation principle, sensitivity and noise performance, etc. In contrast to solid-state seismometer and accelerometer, MET based motion sensors detect the relative movement of the liquid proof-mass to the fixed electrodes. The advantages of the MET motion sensors include: high shock force tolerance, independence of installation angle and low self-noise in low frequency range. These advantages are very favorable for space exploration, so in Chapter 3, the micro MET based seismometer for planetary exploration developed by miniaturizing the traditional MET seismometer using MEMS micro-fabrication techniques is described in detail. The micro-fabrication process involves FIB to finely mill the micro-channels which allow sharp and smooth channel sidewalls. In addition to the advantages of MET, the fabricated device by MEMS techniques has very small size, light weight, and is easy to optimize. In Chapter 4, two alternative fabrication methods for the micro MET seismometer using SOI wafers are

described. These processes enable batch fabrication of the device and increase the number and diameter of the channels, leading to improvement of noise performance and stronger supporting strength. Inspired by the advantages of combining MET and MEMS micro-fabrication techniques, a MET based micro accelerometer is also developed and described in Chapter 5. This accelerometer inherits the advantages of combining MET and MEMS, and has simple fabrication process compared to solid-state MEMS capacitive accelerometer. Furthermore, its fabrication process is post-CMOS compatible. Some of the other topics that need to be addressed in future are discussed in the subsequent sections of this chapter.

6.1 Experiment Setup

Here I would like to acknowledge to Dr. Vadim Agafonov and his colleague from the Center of Molecular Electronics, Moscow Institute of Physics and Technology, Moscow, Russia. Our fabricated micro MET seismometers were sent to their institute for packaging and testing. They took so much efforts to provide us with accurate experimental data of our device using their state-of-art measurement system for MET seismometers. We are currently building up our own experiment setup for MET based or other types of seismometers and accelerometers, which would enable us to test our prototype right after fabrication and give us a quick result to guide us on the optimization direction from fabrication point of view.

Our testing setup is shown in Figure 36 and described as follows: a signal generator which can generate a sinusoidal signal with frequency as low as 0.1 Hz is connected with a power amplifier to drive a long-stroke vibration exciter. The DUT (device under test, i.e.

our MET accelerometer) and a reference accelerometer (i.e. ADXL series accelerometer from Analog Device) are sitting back to back on the vibration exciter. The output of DUT is connected to the testing circuits which is in the form of PCB set up isolated from the vibration area in order to cut out distraction. The output from the peer reference accelerometer (with circuits included) and the PCB are both connected to a data acquisition card, so that vibration data can be recorded by the computer (i.e. Labview). By comparing the output data from DUT and the reference accelerometer, the sensitivity of the MET sensor can be calculated. Also by transferring the time domain data to frequency domain, the noise floor can be measured.

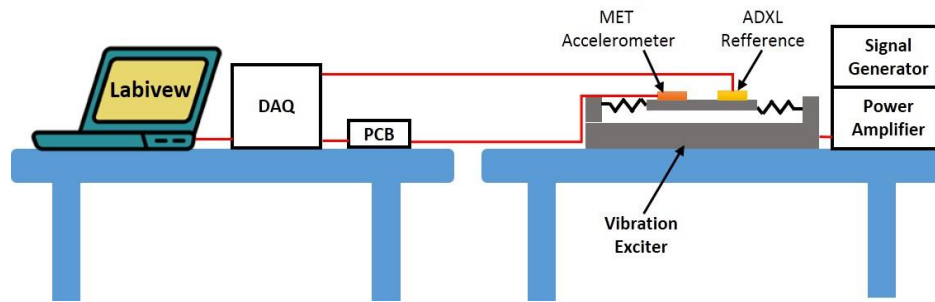


Figure 36. Experiment setup of the MET based micro seismometer/accelerometer.

The circuit prototype for measuring the MET sensor is shown in Figure 37. Basically it consists of two transimpedance amplifiers (AD822, Analog Devices, MA) at the first stage to detect two negative correlative current signals from the two cathodes of the sensor and convert them to voltage signals. A differential amplifier (AD620, Analog Devices, MA) with a configured gain of 10^3 is followed to amplify the difference

between the two converted signals from the transimpedance amplifiers. A final single-ended amplifier followed by a low-pass RC filter is designed as the final stage of the circuits. Signal conditioning and temperature compensation circuits need to be studied in the future.

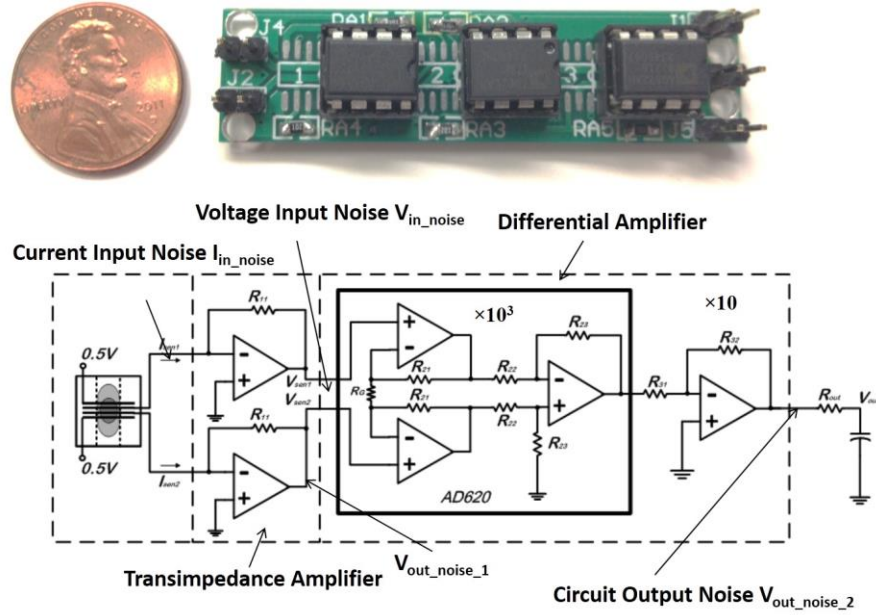


Figure 37. Circuit topology for the measurement of the MET based micro seismometers and accelerometers.

6.2 MET Sensor Packaging

The packaging and assembly of the fabricated MET seismometers are also performed in the Center of Molecular Electronics, Moscow Institute of Physics and Technology, directed by Dr. Vadim Agafonov. Right now we are also planning to develop our own packaging and assembly method at ASU. The packaging and assembly of the micro MET seismometers are described as follows. The chip with sensing cell is

placed between two plastic housing, having a passing through channel. Ends of the channel were covered with flexible chemically inert rubber membranes. All assemble is pressed between two metal flanges. The junctions between chip and plastic parts are sealed with a soft O-ring. The whole assembly prototype is shown on the Figure 38. The ports on the plastic housings are used to fill the internal channel of the sensing element with an electrolyte using vacuum method. The internal volume is first evacuated and then connected to the chamber with an electrolyte staying at normal pressure. After the electrolyte is filled, the ports are sealed with rubber plugs. The packaged device also needs to be assembled inside an air protecting shell.

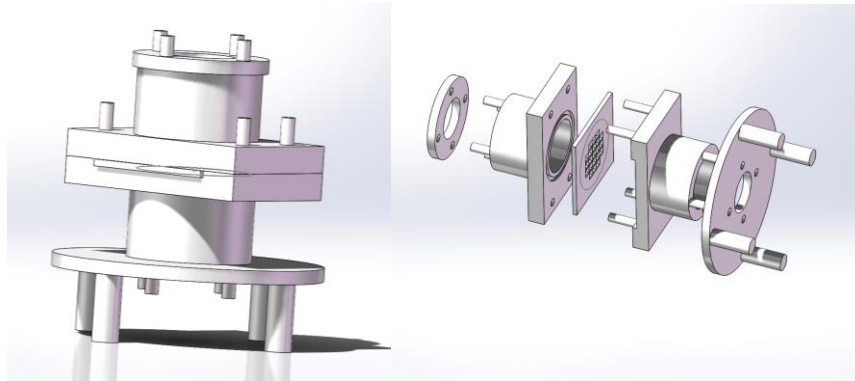


Figure 38. Packaging and assembly prototype of the MET based micro seismometer.

Figure 38 above shows the overview of the whole package. The names of parts in this figure from left to right are: upper cap, upper cylinder, sensor chip, lower cylinder and the base. Notice that all the screw threads or screw nuts are NOT appear on this figure. The upper cap is a flat plate with a big hole on the center and 4 small holes on the side. The 4 small holes are used to the connection of the cap and the cylinder with screw

nuts. The central hole gives the membrane between the cap and cylinder the freedom of deforming. The upper cylinder and the cap are connected the four poles with #1 screw threads on the upper side. For the lower side, a circular channel is carved for the O-ring. The membrane and the O-ring can create a liquid sealed container for the sensor chip. The 4 holes on the base of the upper cylinder are designed for the connection with the lower cylinder. The lower cylinder is similar to the upper one. There is a square slot for holding the sensor chip. 4 poles with threads on the sides of the slot is used to connect with the upper cylinder. Base is like the upper cap. The central hole and four holes aside have the same function as the upper cap. Besides, there are four poles on the bottom which could help the whole package stands on the experiment platform.

6.3 Theoretical Study of MET Principle

This thesis focuses on the development of various fabrication methods to improve the performance of the MET based micro seismometers and accelerometers based on basic understanding of MET theory. However, the theoretical analysis of the working principle of MET based on complex electrochemical and hydrodynamic theory is still a blank, especially the critical size of MET device is scaled down to microns. It would be necessary to use multiphysics FEA simulation (i.e. Comsol Multiphysics) to analyze the behavior of the micro MET sensors, so that the simulation results could help to direct the optimization direction of our fabrication. It would also help us to explore some hidden phenomenon.

REFERENCES

- [1] J. Havskov and G. Alguacil, *Instrumentation in Earthquake Seismology*, Springer, 2004.
- [2] Sleeswyk AW, Sivin N, “Dragons and toads: the Chinese seismoscope of BC. 132”, *Chinese Science* 6: 1–19, 1983.
- [3] Needham, J., *Science and Civilization in China, Volume 3: Mathematics and the Sciences of the Heavens and the Earth*, Cambridge: Cambridge University Press. pp. 626–635, 1959.
- [4] W. Lowrie, *Fundamentals of Geophysics*, Cambridge University Press, 1997.
- [5] A. U. Vallina, *Principles of Seismology*, Cambridge University Press, 1999.
- [6] P. M. Shearer, *Introduction to Seismology*, Cambridge University Press, 1999.
- [7] Magnitude 9.0 – Near The East Coast Of Honshu, Japan, United States Geological Survey (USGS), 5 April 2011.
- [8] New USGS number puts Japan quake at 4th largest. CBS News. Associated Press. 14 March 2011.
- [9] K.-H. Barth, "The Politics of Seismology: Nuclear Testing, Arms Control, and the Transformation of a Discipline," *Social Studies of Science*, vol. 33, pp. 743-781, 2003.
- [10] Lammlein, D.R., “Lunar seismicity and tectonics”, *Physics of the Earth and Planetary Interiors* 14, 224-274, 1977.
- [11] Dunnebier, F.K., Sutton, G.H., “Thermal moonquakes”, *Journal of Geophysical Research* 79, 4351-4364, 1974.
- [12] Dunnebier, F.K., *Moonquakes and meteoroids: Results from the Apollo passive seismic experiment short-period data*, Ph.D. dissertation, University of Hawaii, Honolulu, 1972.
- [13] A. Fagan, C.R. Neal, L. Salvati, S. Sakimoto, Y. Nakamura and J. Weinberg, “The case for a long-lived global lunar geophysical network – 1: seismic data”, *Lunar and Planetary Science Conference XXXVIII*, 2416 (2007).
- [14] C.R. Neal, “Future lunar science opportunities – What’s left to be done?”, *Lunar and Planetary Science Conference XXXIX*, 1190 (2008).
- [15] G. Streckeisen AG, Dattlikonerstrasse 5, CH-8422 Pfungen, Switzerland.

- [16] Guralp Systems Limited, 3 Midas House, Reading RG7 8EA, UK
<http://www.guralp.net>.
- [17] Lemkin, M., Boser, B.E., "A three-axis micromachined accelerometer with a CMOS position-sense interface and digital offset-trim electronics," Solid-State Circuits, IEEE Journal of , vol.34, no.4, pp.456-468, Apr 1999.
- [18] Lu, C., Lemkin, M., Boser, B.E. , "A monolithic surface micromachined accelerometer with digital output," Solid-State Circuits, IEEE Journal of , vol.30, no.12, pp.1367-1373, Dec 1995.
- [19] Tseng, Sheng-Hsiang, Michael SC Lu, Po-Chang Wu, Yu-Chen Teng, Hann-Huei Tsai, and Ying-Zong Juang. "Implementation of a monolithic capacitive accelerometer in a wafer-level 0.18 μm CMOS MEMS process." Journal of Micromechanics and Microengineering 22, no. 5 (2012): 055010.
- [20] Wu, Jiangfeng, Gary K. Fedder, and L. Richard Carley. "A low-noise low-offset capacitive sensing amplifier for a 50- $\mu\text{g}/\sqrt{\text{Hz}}$ monolithic CMOS MEMS accelerometer." Solid-State Circuits, IEEE Journal of 39, no. 5 (2004): 722-730.
- [21] Chae, Junseok, Haluk Kulah, and Khalil Najafi. "A monolithic three-axis micro-g micromachined silicon capacitive accelerometer." Microelectromechanical Systems, Journal of 14, no. 2 (2005): 235-242.
- [22] Qu, Hongwei, Deyou Fang, and Huikai Xie. "A monolithic CMOS-MEMS 3-axis accelerometer with a low-noise, low-power dual-chopper amplifier." *Sensors Journal, IEEE* 8, no. 9 (2008): 1511-1518.
- [23] Sun, Chih-Ming, Ming-Han Tsai, Yu-Chia Liu, and Weileun Fang. "Implementation of a monolithic single proof-mass tri-axis accelerometer using CMOS-MEMS technique." *Electron Devices, IEEE Transactions on* 57, no. 7 (2010): 1670-1679.
- [24] Freescale Semiconductor Inc 2010 ± 6 g two axis low-g micromachined accelerometer Datasheet Rev. 0
- [25] Analog Devices Inc. 2011 ADXL203 Precision ± 1.7 g, Dual-Axis iMEMS® Accelerometer *Datasheet Rev. D*
- [26] S. D. Senturia, Microsystem Design, Kluwer Academic Publishers, 2001.
- [27] Analog Devices Inc. 1998 ADXL150 ± 5 g to ± 50 g, Single-Axis iMEMS® Accelerometer *Datasheet Rev. 0*
- [28] Lognonne, P., "Planetary seismology", Annual Review of Earth and Planetary Science 33, 571-604, 2005.

- [29] Y. Suzuki and Y.-C. Tai, "Micromachined high-aspect-ratio parylene beam and its application to low-frequency seismometer," presented at The 16th IEEE International Conference on Micro Electro Mechanical Systems, Kyoto, Japan, 2003.
- [30] Pike, W.T., Kumar, S., "Improved design of micromachined lateral suspensions using intermediate frames", *J. Micromech. Microeng.* Vol.17, no. 8, pp 1680-1694, July 2007.
- [31] Pike, W. T., et al, "Design, fabrication and testing of a micromachined seismometer with nano-G resolution" in International Solid-State Sensors, Actuators and Microsystems Conference (Transducers 2009), 2009, Denver, CO, USA.
- [32] M. J. Usher, "Developments in seismometry," *Journal of Physics E: Scientific Instruments*, pp. 501-507, 1973.
- [33] Oyo Geospace Corporation, 7007 Pinemont Drive, Houston, Texas 77040, USA <http://www.oyogeospace.com>.
- [34] Hurd, R.M., Lane, R.N., "Principles of very low power electrochemical control devices", *J. Electrochem. Soc.*, 104, 727–730, 1957.
- [35] Wittenborn, A.F., "Analysis of a logarithmic solion pressure detector", *J. Acoust. Soc. Am.*, 30, 683–683, 1958.
- [36] Collins, J.L., Richie, W.C., English, G.E., "Solion infrasonic microphone", *J. Acoust. Soc. Am.*, 36, 1283–1287, 1964.
- [37] Larcam, C.W., "Theoretical analysis of the solion polarized cathode acoustic linear transducer", *J. Acoust. Soc. Am.*, 37, 664–678, 1965.
- [38] Lidorenko, N.S., Ilin, B.I., Zaidenman, I.A., Sobol, V.V., Shchigorev, I.G., "An introduction to molecular electronics", *Enegoatomizdat*, 1984.
- [39] Kozlov, V.A.; Korshak, A.N.; Petkin, N.V. Theory of diffusion-type transducers for ultralow electrolyte flow-rates. *Sov. Electrochem.* 1991, 27, 16–21.
- [40] Kozlov, V.A.; Safonov, M.V. Self-noise of molecular electronic transducers. *Tech. Phys.* 2003, 48, 1579–1582.
- [41] Kozlov, V.A.; Terent'ev, D.A. Transfer function of a diffusion transducer at frequencies exceeding the thermodynamic frequency. *Russ. J. Electrochem.* 2003, 39, 401–406.
- [42] Zakharov, I.S.; Kozlov, V.A. Stationary convective diffusion and nonlinear effects in an electrochemical transducer. *Russ. J. Electrochem.* 2003, 39, 397–400.

- [43] Panferov, A.P.; Kharlamov, A.V. Theoretical and experimental study of an electrochemical converter of a pulsing electrolyte flow. *Russ. J. Electrochem.* 2001, 37, 394–398.
- [44] Reznikova, L.A.; Morgunova, E.E.; Bograchev, D.A.; Grigin, A.P.; Davydov, A.D. Limiting current in iodine–iodide system on vertical electrode under conditions of natural convection. *Russ. J. Electrochem.* 2001, 37, 382–387.
- [45] Kozlov, V.A.; Terent'ev, D.A. Frequency characteristics of a spatially-confined electrochemical cell under conditions of convective diffusion. *Russ. J. Electrochem.* 2002, 38, 992–999.
- [46] Leugoud, R.J. Seismic Detection Using Mini Seismometer. In Proceedings of the Monitoring Research Review: Ground-Based Nuclear Explosion Monitoring Technologies, Portsmouth, Virginia, 23–25 September 2008.
- [47] Abramovich, I.A.; Zhu, T. Next Generation Robust Low Noise Seismometer for Nuclear Monitoring. In Proceedings of the Monitoring Research Review: Ground-Based Nuclear Explosion Monitoring Technologies, Portsmouth, Virginia, 23–25 September 2008.
- [48] Huang, H.; Carande, B.; Tang, R.; Oiler, J.; Zaitsev, D.; Agafonov, V.; Yu, H. Development of A Micro Seismometer Based on Molecular Electronic Transducer Technology for Planetary Exploration. In Proceedings of the 26th IEEE International Conference on Micro Electro Mechanical Systems (MEMS 2013), Taipei, Taiwan, 20–24 January 2013.
- [49] Kozlov, V.A.; Agafonov, V.M.; Bindler, J.; Vishnyakov, A.V. Small, Low-Power, Low-Cost Sensors for Personal Navigation and Stabilization Systems. In Proceedings of the 2006 National Technical Meeting of The Institute of Navigation, Monterey, CA, USA, 18–20 January 2006; pp. 650–655.
- [50] Krishtop, V.G.; Agafonov, V.M.; Bugaev, A.S. Technological principles of motion parameter transducers based on mass and charge transport in electrochemical Microsystems. *Russ. J. Electrochem.* 2012, 48, 746–755.
- [51] Agafonov, V.M.; Nesterov, A.S. Convective current in a four-electrode electrochemical cell at various boundary conditions at anodes. *Russ. J. Electrochem.* 2005, 41, 880–884.
- [52] Agafonov, V.M.; Krishtop, V.G. Diffusion sensor of mechanical signals: Frequency response at high frequencies. *Russ. J. Electrochem.* 2004, 40, 537–541.
- [53] Sun, Z.; Agafonov, V.M. Computational study of the pressure-driven flow in a four-electrode rectangular micro-electrochemical accelerometer with an infinite aspect ratio. *Electrochimica Acta* 2010, 55, 2036–2043.

- [54] Sun, Z.; Egorov, E.; Agafonov, V.M. The influence of the boundary condition on anodes for solution of convection- diffusion equation with the application to a four-electrode electrochemical cell. *J. Electroanal. Chem.* 2011, *661*, 157–161.
- [55] Agafonov, V.M.; Zaitsev, D.L. Convective noise in molecular electronic transducers of diffusion type. *Tech. Phys.* 2010, *55*, 130–136.
- [56] EENTEC. Available online: http://eentec.com/EP-300_data.htm (accessed on 8 September 2013).
- [57] R-sensors, LLC. Available online: <http://www.r-sensors.ru/> (accessed on 8 September 2013).
- [58] Leugoud, R. J., Kharlamov, A. V. Second generation of a rotational electrochemical seismometer using magnetohydrodynamic technology. *J Seismological Society.* 2012, *16*, 587–593.
- [59] Don L. Anderson, W. F. Miller, G. V. Latham, Y. Nakamura, M. N. Toksoz, A. M. Dainty, F. K. Duennebier, A. R. Lazarewicz, R. L. Kovach, and T. C. D. Knight, “Seismology on Mars”, *Journal of Geophysical Research*, vol. 82, No. 28, pp. 4524-4546, 1977.
- [60] Lognonné P., D. Giardini, B. Banerdt, J. Gagnepain-Beyneix, A. Mocquet, T. Spohn, J.F. Karczewski, P. Schibler, S. Cacho, W.T. Pike, C. Cavoit, A. Desauter, J. Pinassaud, D. Breuer, M. Campillo, P. Defraigne, V. Dehant, A. Deschamps, J. Hinderer, J.J. Lévêque, J.P. Montagner, J. Oberst, “The NetLander Very Broad band seismometer”, *Planet. Space Sc.*, 48 :1289-1302, 2000.
- [61] H. Huang, B. Carande, R. Tang, J. Oiler, D. Zaitsev, V. Agafonov, and H. Yu, “A micro seismometer based on molecular electronic transducer technology for planetary exploration,” *Appl. Phys. Lett.*, vol. 102, no. 19, pp. 193512-1–193512-4, 2013.
- [62] V. A. Kozlov and M. V. Safonov, “Dynamic characteristic of an electrochemical cell with gauze electrodes in convective diffusion conditions,” *Russian J. Electrochem.*, vol. 40, no. 4, pp. 460–462, 2004.
- [63] Huang, Hai; Mengbing Liang; Rui Tang; Oiler, J.; Hongyu Yu, "Molecular Electronic Transducer-Based Low-Frequency Accelerometer Fabricated With Post-CMOS Compatible Process Using Droplet as Sensing Body," *Electron Device Letters, IEEE* , vol.34, no.10, pp.1304,1306, Oct. 2013.

APPENDIX

FABRICATION PROCESS FLOW

A.1 Micro-fabrication Process for Micro MET Seismometer Involving FIB

Step	Process Name	Description	Material	Parameters
1	LPCVD SiN	Deposite SiN on both sides of a 500 μm silicon substrate	Si, SiN	0.6 μm SiN
2	Photolithography #1	Patterning for 1st electrode	Photoresist AZ4330	2000rpm, 3 μm
3	Metal E-beam deposition	E-beam metal deposition for 1st electrode	Ti/Pt	10nm/100nm
4	Lift-off	Lift-off 1st electrode	Acetone	
5	PECVD SiN	Deposite 1st separation layer	SiN	350 $^{\circ}\text{C}$, 1.0 μm
6	Photolithography #2	Patterning for 2nd electrode	Photoresist AZ4330	2000rpm, 3 μm
7	Metal E-beam deposition	E-beam metal deposition for 2nd electrode	Ti/Pt	10nm/100nm
8	Lift-off	Lift-off 2nd electrode	Acetone	
9	PECVD SiN	Deposite 2nd separation layer	SiN	350 $^{\circ}\text{C}$, 1.0 μm
10	Photolithography #3	Patterning for 3rd electrode	Photoresist AZ4330	2000rpm, 3 μm
11	Metal E-beam deposition	E-beam metal deposition for 3rd electrode	Ti/Pt	10nm/100nm
12	Lift-off	Lift-off 3rd electrode	Acetone	
13	PECVD SiN	Deposite 3rd separation layer	SiN	350 $^{\circ}\text{C}$, 1.0 μm
14	Photolithography #4	Patterning for 4th electrode	Photoresist AZ4330	2000rpm, 3 μm
15	Metal E-beam deposition	E-beam metal deposition for 4th electrode	Ti/Pt	10nm/100nm
12	Lift-off	Lift-off 4th electrode	Acetone	
13	PECVD SiN	Deposite top separation layer	SiN	350 $^{\circ}\text{C}$, 0.6 μm
14	Photolithography #5	Pattern the contact for 4th electrode	Photoresist AZ4330	2000rpm, 3 μm
15	RIE SiN etching	Etch to expose 4th electrode contact	SiN	150W, 22min
16	Photolithography #6	Pattern the contact for 3rd electrode	Photoresist AZ4330	2000rpm, 3 μm
17	RIE SiN etching	Etch to expose 3rd electrode contact	SiN	150W, 50min
18	Photolithography #7	Pattern the contact for 2nd electrode	Photoresist AZ4330	2000rpm, 3 μm
19	RIE SiN etching	Etch to expose 2nd electrode contact	SiN	150W, 70min

20	Photolithography #8	Pattern the contact for 1st electrode	Photoresist AZ4330	2000rpm, 3 μ m
21	RIE SiN etching	Etch to expose 1st electrode contact	SiN	150W, 100min
22	Metal E-beam deposition	Deposit gold layer on 4 contacts to enhance conductivity	Cr/Au	10nm/500nm
23	Photolithography #9	Patterning for gold etching	Photoresist AZ4330	2000rpm, 3 μ m
24	Wet etching	Gold wet etching	Gold etchant	Inspection
25	Wet etching	Chrome wet etching	Chrome etchant	Inspection
26	Parylene-C deposition	Parylene deposition to protect gold traces	Parylene-C	10 μ m
27	Photolithography #10	Patterning for Parylene etching	Photoresist AZ4620	1500rpm, 15 μ m
28	RIE etching of Parylene	Etch Parylene to expose contact pads	Oxygen Plasma	~30min
29	Photolithography #11	Backside alignment patterning for backside DRIE	Photoresist AZ4620	1000rpm, 20 μ m
30	DRIE	Backside DRIE for device releasing	Si	
31	Device release	Release and separate devices		
32	FIB Milling			

A.2 Micro-fabrication Process for Micro MET Seismometer Using Double SOI Substrate

Step	Process Name	Description	Material	Parameters
1	LPCVD SiN	Deposite SiN on both sides of a 500 μm D-SOI substrate	Si, SiN	0.6 μm SiN
2	Bottom Side Pattern	Pattern bottom side SiN by RIE	Si, SiN	0.6 μm SiN
3	Form bottom side cavity	Etch through from bottom side to D-SOI thin film by TMAH anisotropic etching	Si	500 μm Si
4	Remove SiN and SiO ₂ on bottom	Remove SiN on bottom side and SiO ₂ of bottom SOI layer by RIE	SiO ₂ , SiN	2 μm SiO ₂ 0.6 μm SiN
5	Pattern SiN layer	Pattern SiN top layer by RIE	D-SOI, SiN	0.6 μm SiN
6	Apply photoresist	Apply photoresist on bottom to protect from HF	PR AZ4330	
7	1st D-RIE Si etching	Etch through the Si on top SOI layer by D-RIE	D-SOI, Si	5 μm Si
8	HF wet Etching	Remove SiO ₂ on top SOI layer and form 2 μm undercut by HF wet etching	SiO ₂	2 μm SiO ₂
9	2nd D-RIE Si etching	Etch through the Si on bottom SOI layer by D-RIE	D-SOI, Si	5 μm Si
10	Remove SiN on top	Remove SiN top layer by Phosphoric acid	SiN	0.6 μm SiN
11	E-beam Evaporation Pt deposit	Deposit Pt on both side	Pt, Si	0.2 μm Pt
12	LPCVD parylene	Coating 20 μm parylene on top side	Parylene, Si	10 g Parylene
13	Pattern parylene	Pattern parylene for RIE	PR AZ 4620	15 μm
14	Parylene RIE etching	RIE parylene	Parylene	20 μm
15	Wafer Bonding	Bonding two wafers on parylene coated layer	Parylene	230 $^{\circ}\text{C}$, 1000N, 30min